



Reduced graphene oxide-CdS heterostructure: An efficient fluorescent probe for the sensing of Ag(I) and sunset yellow and a visible-light responsive photocatalyst for the degradation of levofloxacin drug in aqueous phase

Manjot Kaur^a, Ahmad Umar^{b,*}, Surinder Kumar Mehta^a, Sushil Kumar Kansal^{c,*}

^a Department of Chemistry and Centre of Advanced Studies in Chemistry, Panjab University, Chandigarh 160014, India

^b Department of Chemistry, College of Science and Arts, and Promising Centre for Sensors and Electronic Devices, Najran University, Najran, 11001, Saudi Arabia

^c Dr. S. S. Bhatnagar University Institute of Chemical Engineering and Technology, Panjab University, Chandigarh 160014, India

ARTICLE INFO

Keywords:

Ag(I) ions
Sunset yellow
Fluorescence sensing
Levofloxacin
Visible light
Photocatalysis

ABSTRACT

Herein, we report the synthesis and characterization of rGO-CdS heterostructure and their utilization as an efficient material for sensing and visible-light driven photocatalytic degradation applications. The heterostructure was synthesized by facile hydrothermal process and characterized by several techniques which exhibited intriguing compositional, morphological, structural, thermal, textural and photo-physical properties. The high resolution transmission electron microscopy (HRTEM) images of the prepared rGO-CdS heterostructure showed the successful deposition of CdS nanoparticles (CdS NPs) on the surface of reduced graphene oxide (rGO) sheets. The synthesized rGO-CdS heterostructure was employed as an outstanding fluorescent sensor for the selective and sensitive detection of heavy transition metal ion; Ag(I) and a synthetic food colorant; sunset yellow (SY). The detection limit of 12.35 μM and 7.89 μM was found to be for Ag(I) and SY, respectively. The prepared rGO/CdS heterostructure was also successfully applied for the photocatalytic degradation of fluoroquinolone antibiotic, levofloxacin (LVX), and food colorant SY under visible-light irradiation. The removal efficiency of 82.7% was obtained for LVX (10 mg/L) using rGO-CdS heterostructure in 60 min under visible-light irradiation. The synthesized heterostructure displayed enhanced photocatalytic decomposition (82.7%) than pure CdS NPs (67.5%) under optimized reaction conditions (0.50 g/L photocatalyst amount, 10 mg/L LVX initial concentration and pH 9.0). Approximate 66% of SY was degraded in 270 min under visible-light using the prepared heterostructure. The scavenger study confirmed the pivotal role of e^- , O_2^- , OH^\bullet and OH^\bullet in the photocatalytic decomposition process. The amended photocatalytic behaviour of the rGO-CdS heterostructure could be accredited to the enhanced visible light harvesting capability, effective charge separation and transportation of photo-generated charge carriers across the heterojunctional interface. To the best of our knowledge, this is the first report till date on the utilization of rGO-CdS heterostructure for the fluorescence sensing of Ag(I) and SY as well as photocatalytic degradation of LVX and SY.

1. Introduction

Cadmium sulphide (CdS), a II–VI group semiconductor material is broadly utilized in different fields, for instance, sensing, imaging, photocatalysis, optoelectronics and photovoltaics because of its excellent visible light harvesting tendency and direct band gap [1–6]. But there are certain limitations associated with this wonderful material such as aggregation, photo-corrosion and weak quantum efficiency due to the high recombination rate of photo-induced charge carriers. These drawbacks can be overcome by several ways which include hybridization with polymers, doping with transition metal ions, heterostructure

formation by coupling with suitable materials and controlling the size, crystal structure and morphology [7–13]. The coupling of pure CdS with carbonaceous materials including graphene and its derivatives is one of the most effective strategies to alter its optical, electronic and catalytic properties. Graphene, a wonderful material exhibits good electrical conductivity, large theoretical specific surface area, high transparency, excellent mechanical flexibility and high chemical stability [14,15]. The heterostructures based on graphene or reduced graphene oxide (rGO) showed extraordinary sensing and photocatalytic applications due to the lower recombination rate of electron-hole pairs, more surface reactive sites, extension in the light absorption region and

* Corresponding authors.

E-mail addresses: ahmadumar786@gmail.com (A. Umar), sushilkk1@pu.ac.in (S.K. Kansal).

<https://doi.org/10.1016/j.apcatb.2018.12.042>

Received 28 September 2018; Received in revised form 7 December 2018; Accepted 15 December 2018

Available online 17 December 2018

0926-3373/© 2018 Elsevier B.V. All rights reserved.

enhanced chemical stability, etc [16–19]. Based on the extraordinary properties and wide applications of graphene based composites, in this paper, rGO/CdS heterostructure was hydrothermally synthesized and exhaustively characterized using multiple analytical and spectroscopic techniques. The prepared heterostructure was employed as an excellent fluorescence probe for the specific and sensitive detection of Ag(I) ions and SY dye and also as a photocatalyst for the photocatalytic degradation of LVX and SY under visible-light irradiation.

Recently, due to huge industrialization and environmental pollution caused by the release of various toxic and hazardous chemicals and other species, extensive research on environmental remediation has received great attention from the scientists [20–22]. Developing new sensing systems and photocatalytic degradation of toxic and hazardous materials are two main environmental remediation processes, which are extensively studied. In this regard, the fabrication of sensing systems for the determination of various species including heavy transition metal ions, biomolecules, food colorants, explosives, hazardous chemicals and pharmaceutical drugs has gained remarkable attention due to their convenient use in environmental, chemical, food, biomedical and clinical fields [23–26]. Up to now, various traditional methods including atomic absorption spectroscopy, voltammetry, inductively coupled plasma-mass spectrometry, capillary electrophoresis, spectrophotometry and flow injection analysis have been widely employed for the sensing purposes [27–31]. However, these instrumental techniques are expensive, complex, time-consuming and require tiresome sample preparation methods. In contrast, fluorescence (FL) spectroscopy has gained significant attraction owing to its high sensitivity, selectivity, rapid response, relatively low cost, easy handling and ability to detect analytes even at minute concentrations [32]. The sensing of heavy transition metal ions using FL spectroscopy has captured utmost importance as these metal ions play an imperative role in different physiological processes. However, the superabundance of these metal ions imposes detrimental effects on the living species due to their long retention period in the environment and high toxicity [33–35]. Among the various transition elements, Ag(I) has been widely applied in electroplating, photographic, coinage, metallurgy, food and pharmaceutical industries. It exhibits strong binding affinity towards amino and sulfhydryl groups and thereby, resulting in the formation of harmful complexes with amino acids, nucleic acids and other substances in the human body. An excessive amount of Ag(I) can also induce detrimental effects on human health ranking from argyria, skin/eyes irritations, cardiac enlargement to damage of liver and kidneys [36–38]. Thus, due to the serious toxic effects of Ag(I), not only to human health but also to other living organisms, it is necessary to develop efficient and effective method for the detection of Ag(I). In this work, we report, *for the first time*, the use of rGO/CdS heterostructure for the fabrication and characterization of highly sensitive FL sensor for the efficient detection of Ag(I) ions.

Similarly, the synthetic dyes are extensively applied in food industries because they exhibit remarkable features such as immense water solubility, color uniformity, low manufacture cost and excellent stability against light, oxygen and pH. Among various dyes, sunset yellow (SY), also known as E110 in Europe, is commonly used in different food products such as candies, bakery products, carbonated beverages, meat products and spicy snacks for making the food attractive and appetitive. However, the existence of azo group (N=N) and aromatic ring in the structure of SY is accountable for several health problems such as diarrhoea, gastric upset, urticaria, angioedema, migraines, hepatocellular damage, kidney injury, eczema, anxiety, cancer, asthma and attention deficit hyperactivity disorder (ADHD), etc [39–42]. The Food and Agricultural Organization (FAO) and World Health Organization (WHO) have recommended daily dose of SY lower than 2.5 mg/kg due to the potential carcinogenicity and pathogenicity associated with this synthetic food colorant [43]. Because of the harmful effects of synthetic colorants, several efforts were made to fabricate food colorant sensors and reported in the literature [44–49].

Song et al. [44] reported the sensing of SY using multi walled carbon nanotubes modified glassy carbon electrode. Detection of allura red based on the composite of poly (diallyl dimethyl ammonium chloride) functionalized graphene and nickel nanoparticles modified electrode was presented by Yu et al. [45]. Majidi et al. [46] demonstrated the use of carbon nanotube-ionic liquid (CNT-IL) heterostructure modified sol-gel derived carbon-ceramic electrode for simultaneous determination of SY and tartrazine in food samples and reported in the literature. Using boron-doped diamond electrodes, Medeiros et al. [47] fabricated and reported an electrochemical sensor for the simultaneous determination of synthetic colorants in food samples. There were other reports as well which demonstrate the fabrication of sensors for the determination of synthetic colorants [48,49]. However, most of the reported sensors were fabricated based on electrochemical processes. It is important to note that in the electrochemical sensing, the detection electrodes are highly influenced by variations of temperature, humidity and ionic concentrations which limit the shelf-life of the device. Moreover, the electrochemical sensing is also time consuming because several complicated steps are required in the fabrication of functionalized electrodes. Therefore, an efficient sensing system should be developed which can detect SY in lower concentrations. The FL sensing has several advantages as it is easy to perform, rapid response, minimal sample preparation and possesses better selectivity as compared to electrochemical methods. Thus, herein, *for the first time*, an effective and efficient FL sensor for the detection of SY was fabricated based on prepared rGO/CdS heterostructures.

Similarly, the pharmaceutical compounds, for instance, synthetic antibiotics are extensively utilized in human and veterinary medicines owing to their peculiar features such as high potency, ease of bioavailability, low cost and broad activity spectrum [50–52]. Fluoroquinolones (FQs) constitutes of the third largest group of non-steroidal antibiotics and it has been reported that in 2009, these accounted for 17% of the global market share with the trade of 7.1 billion \$ [53]. Levofloxacin ($C_{18}H_{20}FN_3O_4$; LVX), the third generation FQ antibiotic has been widely employed to cure pneumonia, chronic bronchitis and urinary tract infections [52,54]. The partial metabolism of antibiotics in the human body is responsible for the development of pathogen resistant bacteria and thereby, leads to the disruption of endocrine system [55]. Therefore, the complete removal of these recalcitrant pollutants from the aquatic environment using efficient and sustainable methods is highly desired. Thus, using the prepared rGO-CdS heterostructure as photocatalyst, we report *for the first time*, the efficient and effective degradation of LVX under visible-light irradiation.

In this paper, rGO-CdS heterostructure was synthesized and characterized using multiple analytical and spectroscopic techniques and used as potential material for the fabrication of efficient FL sensor for the detection of Ag(I) ions and SY dye. Moreover, the heterostructure was successfully utilized for the photocatalytic decomposition of LVX and SY under visible light irradiation. The effect of different operational parameters such as pH, catalyst dose, initial substrate concentration and the role of various reactive oxygen species towards the degradation process has been fully explored. The prepared heterostructure displayed enhanced photocatalytic performance than pure CdS NPs and underlying sensing and photocatalytic degradation mechanisms have been proposed.

2. Experimental details

2.1. Reagents

All the reagents used in the present work were of analytical grade and utilized as received without any further purification. Graphite (GR, 99.5%), thioacetamide (C_2H_5NS , 99%), barium sulphate ($BaSO_4$, 97%), terephthalic acid (TA; $C_8H_6O_4$, 98%), sodium chloride (NaCl, $\geq 99\%$), L-ascorbic acid (AA; $C_6H_8O_6$, 99%), dopamine hydrochloride (DA; $C_8H_{11}NO_2 \cdot HCl$, 98%), tartrazine (TZ; $C_{16}H_9N_4Na_3O_9S_2$) and SY

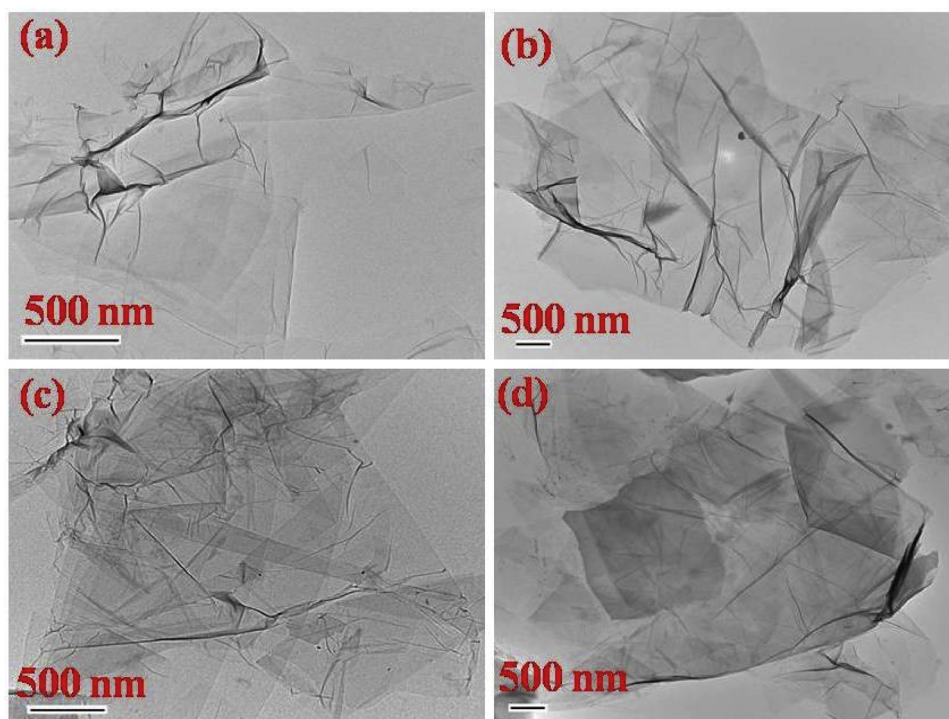


Fig. 1. Typical (a–d) TEM images of prepared GO sheets.

($C_{16}H_{10}N_2Na_2O_7S_2$) were bought from Himedia, India. Cadmium acetate dihydrate ($Cd(CH_3COO)_2 \cdot 2H_2O$, $\geq 98\%$), sulphuric acid (H_2SO_4 , 98%), hydrochloric acid (HCl, 36.5–38%), copper acetate monohydrate ($Cu(CH_3COO)_2 \cdot H_2O$, $\geq 98\%$), *p*-benzoquinone (BQ; $C_6H_4O_2$, $\geq 98\%$), lead nitrate ($Pb(NO_3)_2$, $\geq 98.5\%$), strontium nitrate ($Sr(NO_3)_2$, 99%), cerium nitrate hexahydrate ($Ce(NO_3)_6 \cdot 6H_2O$, $\geq 99\%$), potassium permanganate ($KMnO_4$, $> 98.5\%$), potassium nitrate (KNO_3 , $\geq 99\%$), potassium iodide (KI, $\geq 99\%$), mercury sulphate ($HgSO_4$, $\geq 99\%$), sodium hydroxide (NaOH, $\geq 97\%$), ethanol (C_2H_5OH , $> 99\%$), hydrogen peroxide (H_2O_2 , 30%) and formic acid (FA; $HCOOH$, ≥ 98 –100%) were purchased from Merck, India. Sodium nitrate ($NaNO_3$, 98%) and silver nitrate ($AgNO_3$, 99.8%) were procured from Fischer Scientific, India. Nickel sulphate hexahydrate ($NiSO_4 \cdot 6H_2O$, 99%) was obtained from Sigma Aldrich, India. The target antibiotic LVX was taken from Saurav chemicals limited, Derabassi, India. Stock solutions were prepared using double distilled water and pH was maintained by using 0.1 M HCl and 0.1 M NaOH solutions on a Mettler Toledo pH-meter (FEP 20).

2.2. Synthesis of graphene oxide (GO)

GO was synthesized from natural GR powder using modified Hummer's method [56,57]. In a typical procedure, 3 g of GR powder and 1.5 g of $NaNO_3$ were added to 75 mL of concentrated H_2SO_4 (98%) and the suspension was placed in an ice bath and stirred for 45 min. Consequently, 9 g of $KMnO_4$ was gradually added and the reaction was continued for 2 h. Later, the solution was removed from ice bath and later heated at $40^\circ C$ for 1 h followed by the addition of 150 mL of distilled water in the time period of 1.5 h. Afterwards, the temperature was raised to $95^\circ C$ for 30 min and the mixture was diluted with 200 mL of distilled water under continuous magnetic stirring. Further, 30 mL of H_2O_2 (30%) was added in 30 min with simultaneous heating at $95^\circ C$. The mixture was again stirred for 13.5 h until effervescence was ceased and brilliant yellow suspension was obtained. The solution was centrifuged at 7000 rpm for 45 min and the supernatant was decanted. The brown precipitates were obtained and dispersed in 10% HCl solution. The suspension was vigorously stirred followed by the centrifugation at

7000 rpm. The obtained product was then re-dispersed in distilled water and the solution was again centrifuged. The washing procedure with distilled water has been repeated several times and the brown colored product was retrieved by centrifugation separation. Finally, the product was dried in an electric oven.

2.3. Preparation of rGO-CdS heterostructure

rGO-CdS heterostructure was synthesized by facile hydrothermal process [58,59]. In a typical synthesis procedure, 133 mg of as-prepared GO was dispersed in 25 mL of distilled water under sonication until achieving the homogeneous suspension of GO solution. 20 mmol of $Cd(CH_3COO)_2 \cdot 2H_2O$ was added to 75 mL of ethanol and the solution was magnetically stirred for 5 h. In a separate beaker, 30 mmol of C_2H_5NS was dissolved in 25 mL of distilled water. Both $Cd(CH_3COO)_2 \cdot 2H_2O$ and C_2H_5NS solutions were mixed vigorously and stirred and GO suspension was added to the reaction mixture under sonication. After required sonication time, the suspension was then transferred to a teflon-lined stainless steel autoclave and heated at $170^\circ C$. After completing the reaction in 20 h, the autoclave was allowed to cool at room-temperature and obtained precipitates were filtered and thoroughly washed with ethanol-water mixture for several times and finally dried in an electric oven. During the synthetic procedure, reduction of GO was achieved and pure CdS NPs were obtained using the same synthesis method without the addition of GO.

2.4. Characterizations

The synthesized samples were exhaustively characterized by different analytical and spectroscopic techniques. The X-ray diffraction (XRD) patterns were recorded on a PANalytical X'Pert PRO diffractometer using $Cu K\alpha$ radiation at 2θ of 5° – 80° . The functional groups were identified using Fourier transform infrared (FTIR) spectroscopy acquired on a Nicolet iS50 FTIR spectrophotometer (Thermo Scientific) in the range of 400 – 4000 cm^{-1} . The surface composition of as-prepared rGO-CdS heterostructure was analyzed using X-ray photoelectron spectroscopy (XPS) on a Omicron ESCA (electron spectroscopy

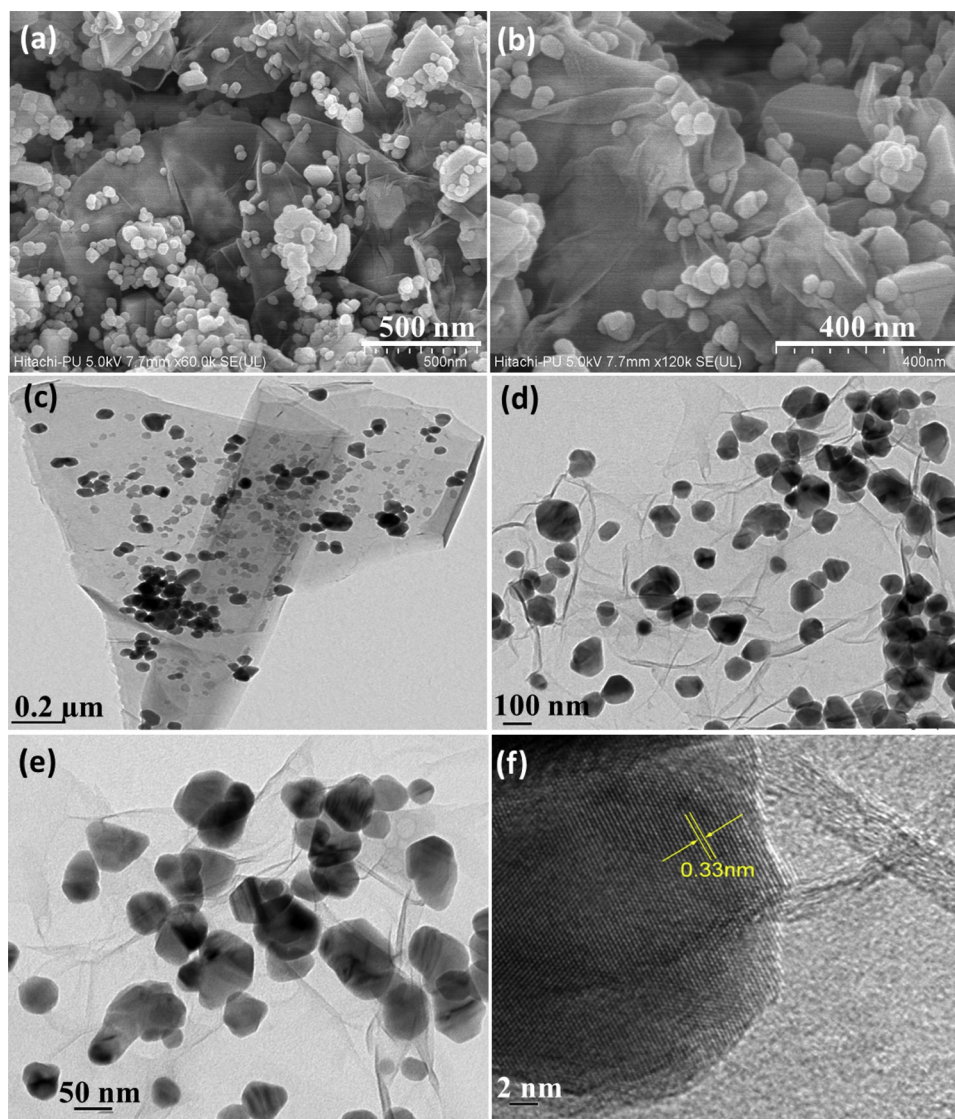


Fig. 2. Typical (a, b) FESEM images, (c–e) TEM images, and (f) HRTEM image of the synthesized rGO-CdS heterostructure.

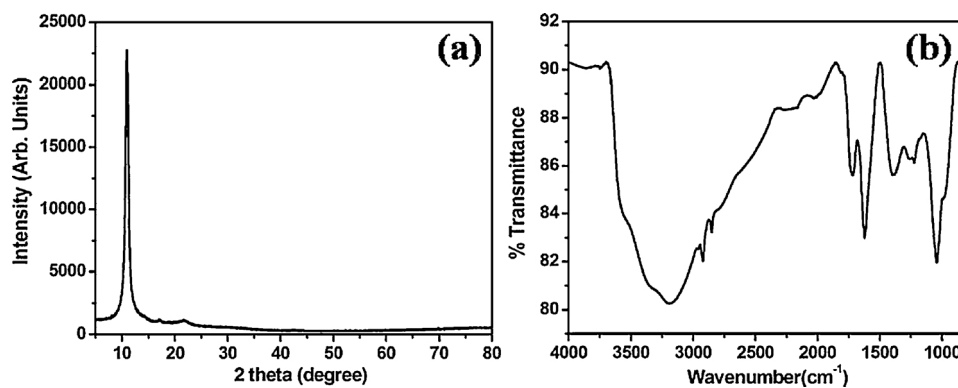


Fig. 3. Typical (a) XRD and (b) FTIR pattern of prepared GO sheets.

for chemical analysis) from Oxford instrument, Germany. The angle between analyzer and source was approximately 85° and Al anode was employed with energy of 1486.7 eV. Thermogravimetric analysis (TGA) was performed on a SDT Q600-TA instrument. The samples were heated under nitrogen atmosphere at a heating rate of $20^\circ\text{C}/\text{min}$. The transmission electron microscopy (TEM) images were taken on a Hitachi H-7500 electron microscope. The high resolution transmission electron

microscope (HRTEM) images of rGO-CdS heterostructure were captured on a FEI Technai F20 instrument. The surface morphology of rGO-CdS heterostructure was observed by recording the field emission scanning electron microscopy (FESEM) images on a Hitachi-8010 microscope. The specific surface area was analyzed using N_2 adsorption/desorption isotherm on a Quantachrome Nova 2000e BET analyzer and prior to BET measurements, the sample was degassed at 150°C for 6 h. The

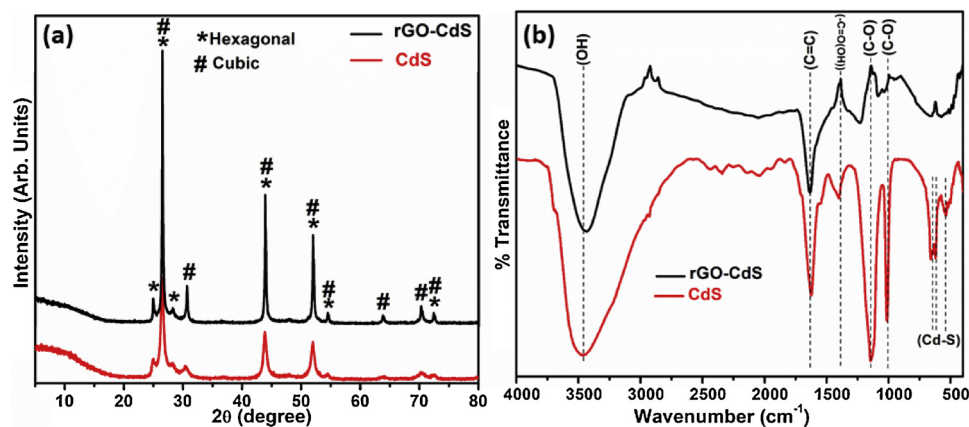


Fig. 4. Typical (a) XRD and (b) FTIR spectra of pure CdS NPs and rGO-CdS heterostructure.

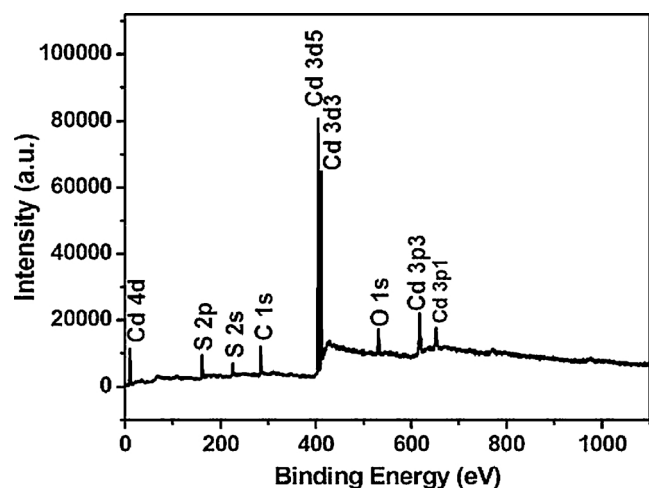


Fig. 5. Wide scan XPS spectrum of the prepared rGO-CdS heterostructure.

Raman spectrum of the synthesized rGO-CdS heterostructure was measured using 785 nm laser as an excitation wavelength on a Renishaw (in via) microscope. The FL emission spectra were recorded at a room temperature on a Hitachi F-7000 FL spectrophotometer. The ultraviolet-visible diffuse reflectance (UV-vis DRS) spectra were obtained using BaSO₄ as a standard reflectance material on a UV-2600, Shimadzu UV-vis spectrophotometer in the wavelength range of 200–800 nm. The ultraviolet-visible (UV-vis) absorbance spectra were measured on a Systronics-2202 UV-vis spectrophotometer. The mineralization extent was found with respect to the reduction in total organic carbon (TOC) content and TOC measurements were performed on a TOC-L CPN Shimadzu analyzer. The formation of reaction intermediates for the degradation of LVX over rGO-CdS heterostructure was studied using XEVO G2XS QTOF model for mass and Acquity UPLC H class for LC, Waters India Pvt Ltd instrument. The column specifications are: Acquity BEH C18 1.7 μ m 2.1*50 mm column and mobile phase composition of A-0.1% formic acid in water and B-100% ACN were chosen for the analysis. The volume of injected sample was 1 μ L with the syringe pump flow rate of 0.6 mL/min and the mass spectra were

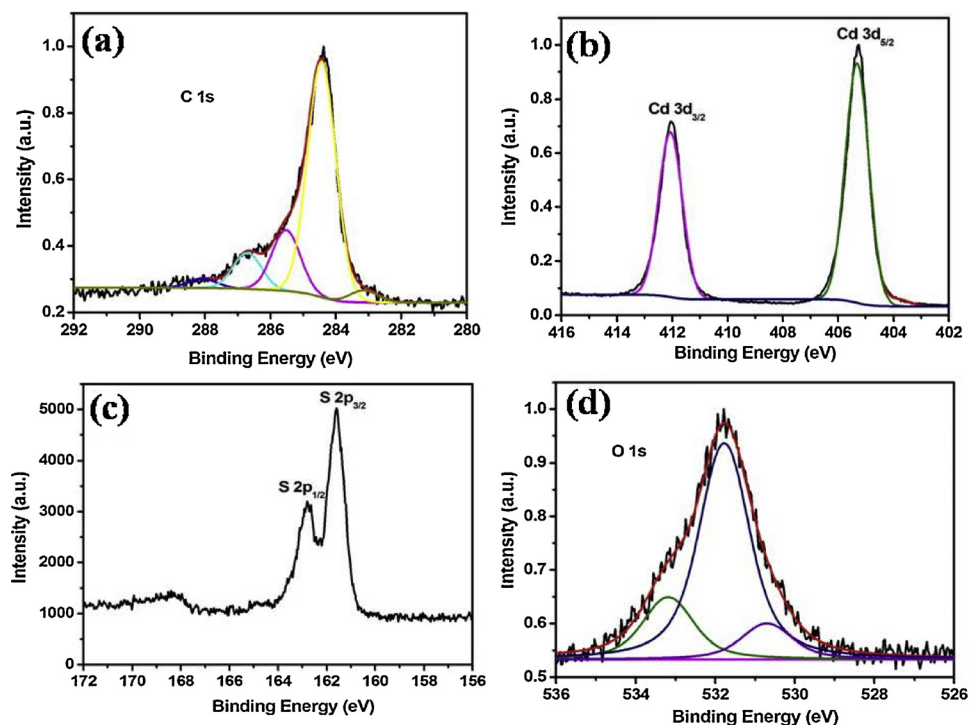


Fig. 6. High resolution XPS survey of (a) C 1s spectrum, (b) Cd 3d spectrum, (c) S 2p spectrum and (d) O 1s spectrum.

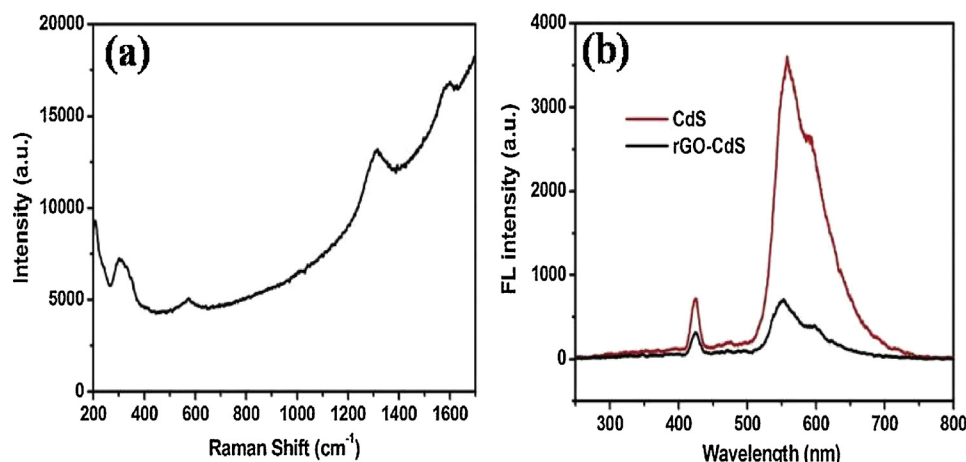


Fig. 7. Typical (a) Raman spectrum and (b) FL spectra of the synthesized rGO-CdS heterostructure.

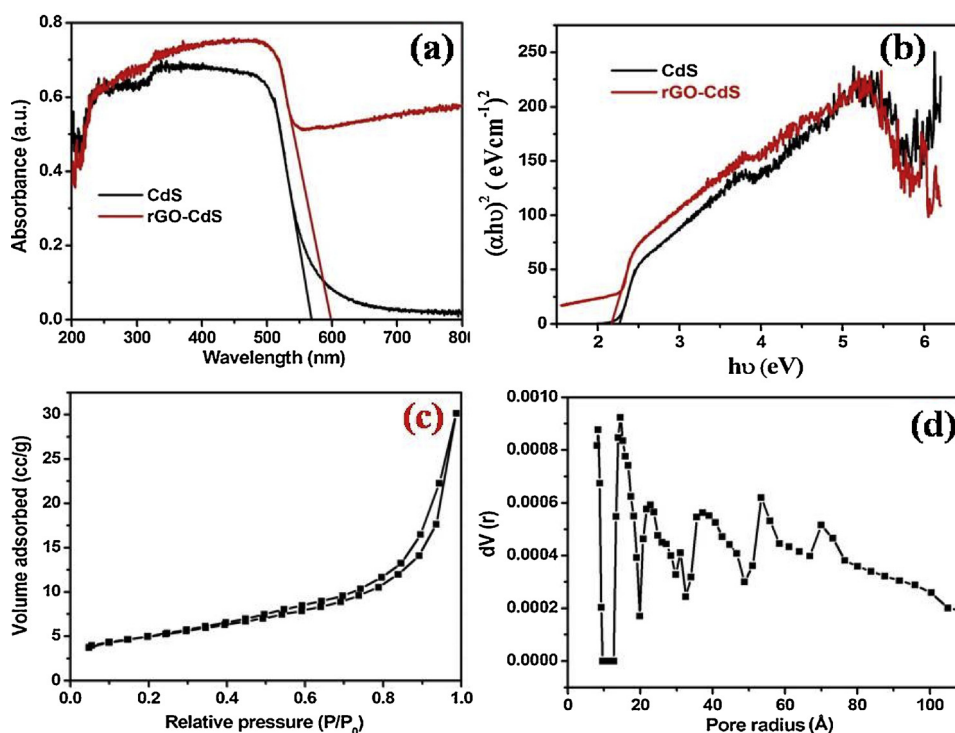


Fig. 8. Typical (a) UV-DRS, (b) Tauc plot, (c) BET adsorption-desorption isotherm curve and (d) pore radius distribution of the synthesized rGO-CdS heterostructure.

scanned in the range of $m/z = 100$ –1000.

2.5. FL sensing of Ag(I) and SY using rGO-CdS heterostructure

The prepared rGO-CdS heterostructure was dispersed in ethanol to obtain the concentration of 0.20 mg/mL and stock solutions of different interfering substances were prepared in double distilled water. The sensing experiment was performed by adding aqueous solution of different species including AA, Cd, Ce, Cu, DA, Ag, Hg, K, Ni, Pb, Sr, SY and TZ (concentration: 100 mM, volume: 1 mL) to rGO-CdS heterostructure solution (concentration: 0.20 mg/mL, volume: 1 mL). The FL spectra of rGO-CdS heterostructure were recorded in the absence and presence of various interfering species. Furthermore, the specificity of the prepared sensor towards the detection of Ag(I) and SY was evaluated with the addition of 1 mL of different competitive substances (100 mM) to the solution containing 1 mL of rGO-CdS heterostructure (0.20 mg/mL) and 1 mL of Ag(I) or SY (100 mM). The sensitivity of the designed sensor was found by adding different concentrations of Ag(I) or SY into

the stock solution of rGO-CdS heterostructure (concentration: 0.20 mg/mL, volume: 1 mL). The FL sensing of Ag(I) and SY was performed under the following experimental conditions: excitation wavelength: 210 nm; emission wavelength: 545 nm; PMT voltage: 750 nm; response time: 0.5 s, excitation and emission slit width: 5 nm. All the FL experiments were carried out at a room temperature.

2.6. Photocatalytic degradation of LVX using rGO-CdS heterostructure under visible light irradiation

The photocatalytic performance of the prepared rGO-CdS heterostructure was assessed for the decomposition of LVX in the presence of visible light irradiation. A 85 W Oveva CFL bulb having wavelength in the range of 450–650 nm with intensity of 4150 lumens was employed in all the photocatalytic reactions. The photocatalytic decomposition reactions were conducted in a chamber equipped with a cylindrical batch reactor and the constant temperature of 25 °C was maintained by circulation of water through an external jacket. A specific amount of the

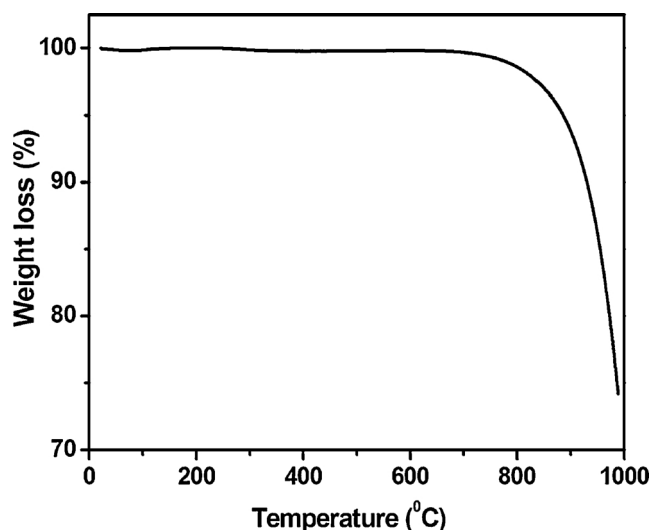


Fig. 9. TGA curve of as-prepared rGO-CdS heterostructure.

synthesized rGO-CdS heterostructure was suspended in 100 mL of LVX solution. The suspension was placed in the dark environment for 30 min under constant magnetic stirring to establish adsorption/desorption equilibrium between LVX solution and the prepared heterostructure prior to the visible light irradiation. The solution was then subjected to visible light and 2.5 mL of aliquots were sampled at desired time intervals. The photocatalyst was separated by filtration through 0.45 μm Chromafil syringe filter and the absorbance of the filtered solution was analyzed at $\lambda_{\text{max}} = 286 \text{ nm}$ using UV-vis spectrophotometer. The degradation efficiency was calculated from the following equation:

$$\text{Degradation (\%)} = (1 - C/C_0) \times 100$$

where, C_0 is the initial concentration of LVX and C is the residual concentration of LVX at specific time intervals when subjected to visible light illumination.

The role of reactive oxygen species towards the photocatalytic removal of LVX was ascertained by adding 0.01 M of NaCl (scavenger for holes; h^+), -FA (scavenger for electrons; e^-), KI (scavenger for h^+ and surface bounded hydroxyl radicals; $\cdot\text{OH}_s$) and 1 mM of BQ (scavenger for superoxide anion radicals; $\text{O}_2^{\cdot-}$) to the LVX solution prior to the addition of the rGO-CdS heterostructure.

The generation of $\cdot\text{OH}$ during the photocatalytic reaction was measured using FL technique by employing TA as a probe molecule. In the brief procedure, 50 mg of the synthesized rGO-CdS heterostructure was dispersed in $5 \times 10^{-4} \text{ M}$ TA and $2 \times 10^{-3} \text{ M}$ NaOH solution and then exposed to visible light irradiation. Approximate 2.5 mL of the photo-reacted suspension was taken at distinct time intervals and

filtered through 0.45 μm Chromafil syringe filter. The filtrates were measured on a FL spectrophotometer in the range of 350–550 nm at $\lambda_{\text{exc}} = 325 \text{ nm}$.

3. Results and discussion

3.1. Morphological, structural and optical characterizations

The structural information and microscopic morphologies of prepared samples were examined using TEM technique. Fig. 1(a–d) exhibits the TEM images of prepared GO. The exfoliated GO displayed sheets like morphology with wrinkled, transparent and folded surface.

The morphology of the synthesized rGO-CdS heterostructure was examined by FESEM and TEM equipped with high-resolution TEM (HRTEM). Fig. 2(a) and (b) exhibit the typical FESEM images of prepared rGO-CdS composite which clearly revealed that small CdS NPs are decorated on the surfaces of rGO nanosheets. The typical sizes of the NPs are in the range of $40 \pm 5 \text{ nm}$ while some bigger NPs are also seen.

Fig. 2(c–e) demonstrate the typical TEM images of synthesized rGO-CdS composite which confirmed the full consistency with the observed FESEM images in terms of morphologies and dimensionalities of the synthesized material. Interestingly, it was observed that CdS NPs are uniformly decorated on the surface of GO sheets, confirming the formation of heterostructure. Also, it was found that CdS NPs were firmly bound to the surface of GO sheets even after substantial ultra-sonication process which depicted the strong intimate interfacial contact between the two components of the heterostructure. Fig. 2(f) shows the HRTEM image of the synthesized rGO-CdS heterostructure and exhibited an interplanar spacing of 0.33 nm which can be indexed to the (111) crystallographic plane of CdS NPs. Therefore, the HRTEM images clearly demonstrated the formation of heterojunction between CdS NPs and rGO sheets which is beneficial in the charge transportation process across the interface and hence, enhance the sensing and photocatalytic activities of the prepared heterostructure.

The phase purity and crystalline properties of the synthesized samples were examined by XRD technique. Furthermore, FTIR spectroscopy was employed for the identification of different functional groups. Fig. 3(a and b) exhibits the XRD and FTIR pattern of prepared GO sheets. The XRD diffractogram of GO displayed a strong diffraction peak at $2\theta = 10.9^\circ$ which can be assigned to the (002) plane of GO [3]. The FTIR spectrum of GO displayed absorption peaks at 3194, 2922, 2853, 1717, 1618, 1393, 1231 and 1040 cm^{-1} . The peak at 3194 cm^{-1} was ascribed to the stretching vibrations of H–O–H band of adsorbed water molecules [13]. A peak at 1618 cm^{-1} was assigned to the existence of C=C bonding. The absorption peaks at 2922 and 2853 cm^{-1} were related to the asymmetric and symmetric stretching vibrations of CH_2 group, respectively [60]. A peak at 1717 cm^{-1} corresponded to the C=O stretching vibrational mode of carboxyl group [60,61]. The bands located at 1231 and 1393 cm^{-1} revealed the

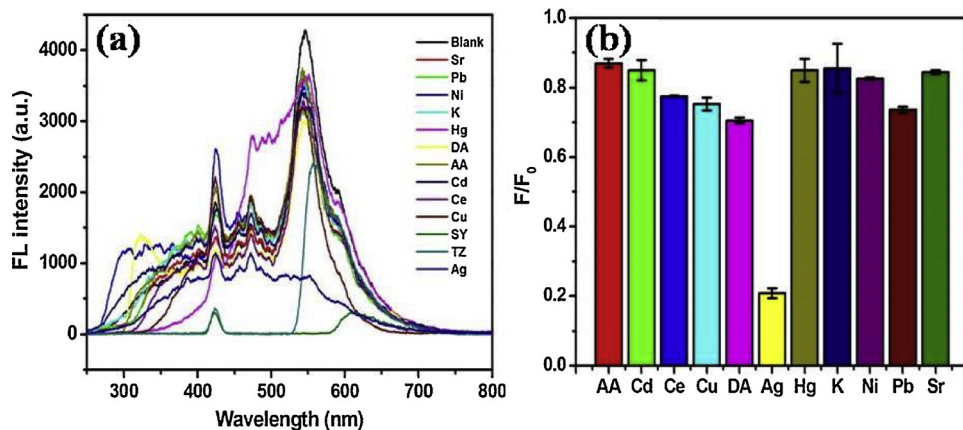


Fig. 10. (a) FL response of the prepared rGO-CdS heterostructure (concentration: 0.20 mg/mL, volume: 1 mL) in the presence of different metal ions and organic compounds (concentration: 100 mM, volume: 1 mL) and (b) Bar graph illustrating the effect of different interfering substances on the FL intensity of rGO-CdS heterostructure. The error bars are based on standard deviations of two measurements.

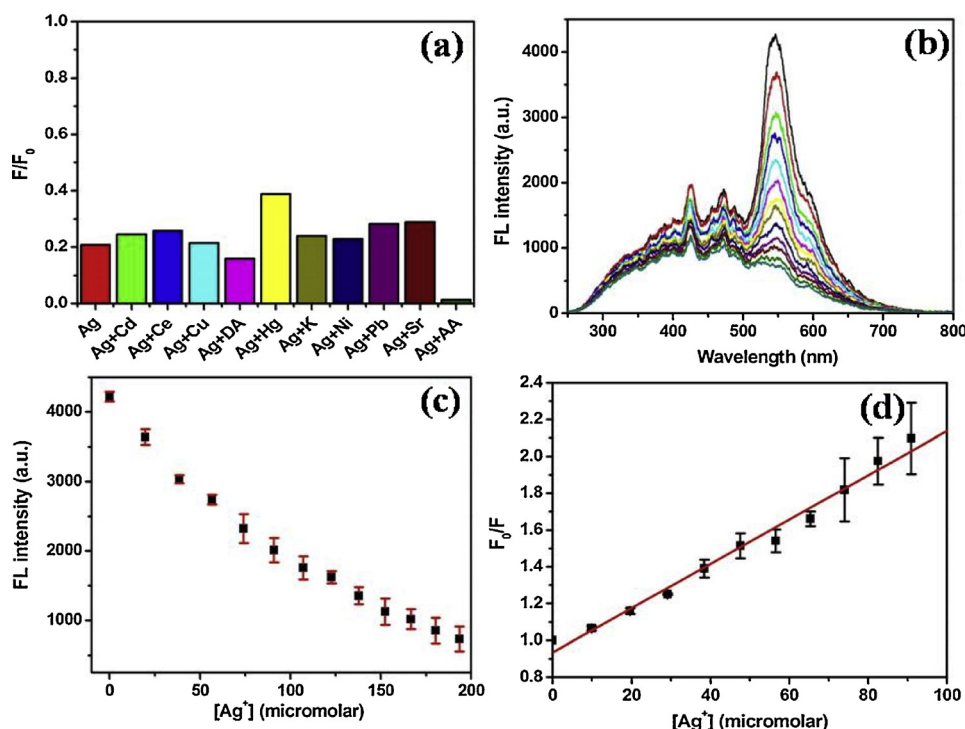


Fig. 11. (a) FL behaviour of the rGO-CdS heterostructure (concentration: 0.20 mg/mL, volume: 1 mL) in the presence of Ag(I) (concentration: 100 mM, volume: 1 mL) and other interfering species (concentration: 100 mM, volume: 1 mL), (b) FL emission spectra of rGO-CdS heterostructure with respect to increased concentration of Ag(I) (from top to bottom: 0, 19.6, 38.46, 56.6, 74.07, 90.9, 107.14, 122.8, 137.93, 152.54, 166.66, 180.32, 193.54 μ M), (c) Variation of FL intensity of rGO-CdS heterostructure on addition of different concentrations of Ag(I) and (d) Relationship between F_0/F and Ag(I) concentration (where F_0 and F corresponds to the FL emission intensity values at 545 nm in the absence and presence of Ag(I)). The error bars correspond to the standard deviation based on duplicate experiments.

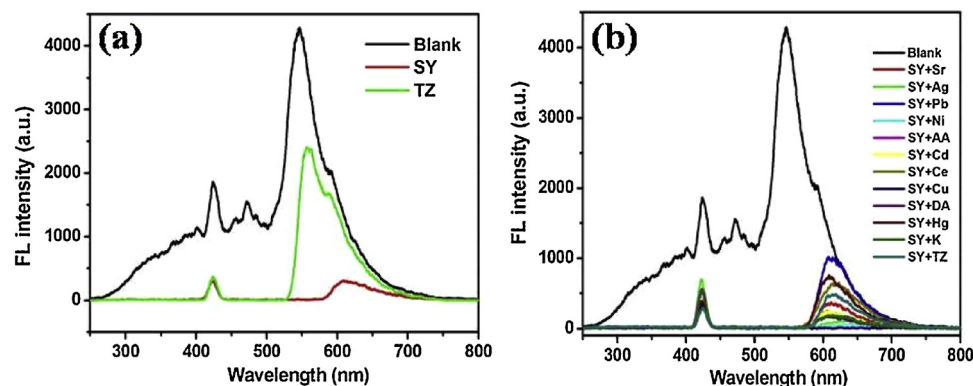


Fig. 12. (a) FL emission curves of the synthesized rGO-CdS heterostructure (concentration: 0.20 mg/mL, volume: 1 mL) in the presence and absence of synthetic food colorants (SY and TZ) (concentration: 100 mM, volume: 1 mL) and (b) Change in FL emission intensity of rGO-CdS heterostructure (concentration: 0.20 mg/mL, volume: 1 mL) with the addition of SY (concentration: 100 mM, volume: 1 mL) and other competitive substances (concentration: 100 mM, volume: 1 mL).

presence of phenolic C–OH and carboxyl O–H stretching vibrations [8]. The peak centered at 1040 cm^{-1} was associated to the C–O stretching vibrations of the epoxy functional group [60,8].

The XRD diffractograms of pure CdS NPs and rGO-CdS heterostructure are depicted in Fig. 4(a). The XRD spectrum of synthesized CdS NPs displayed distinctive diffraction peaks at $2\theta = 24.9^\circ$, 26.5° , 28.2° , 30.6° , 43.9° , 51.9° , 54.4° , 63.7° , 70.3° and 72.4° . The peaks at 26.5° , 30.6° , 43.9° , 51.9° , 54.4° , 63.7° , 70.3° and 72.4° can be ascribed to the (111), (200), (220), (311), (222), (400), (331) and (420) lattice planes of cubic phase, respectively in accordance with the JCPDS card no. 89-0440. Also, the diffraction peaks at 24.9° , 26.5° , 28.2° , 43.9° , 51.9° , 54.4° and 72.4° can be assigned to the (100), (002), (101), (110), (112), (004), and (114) crystallographic planes of hexagonal phase of CdS, respectively (JCPDS card no. 80-0006) [1]. The XRD diffractogram of rGO-CdS heterostructure showed full consistency with that of pure CdS NPs. The XRD pattern of pure CdS NPs and rGO-CdS heterostructure exhibited that CdS NPs was composed of crystal mixture of cubic and hexagonal phases [1]. Also, the peak of exfoliated GO at $2\theta = 10.9^\circ$ was disappeared during the formation of rGO-CdS heterostructure with the appearance of new diffraction peaks at $2\theta = 23.8^\circ$ and $2\theta = 43.5^\circ$, verifying the hydrothermal reduction of GO as shown in Fig. S1. Therefore, the XRD diffractogram indicated the complete

exfoliation of GR powder and the successful reduction of GO [62–64]. The XRD spectrum of as-synthesized rGO-CdS heterostructure exhibited no diffraction reflection planes associated with rGO due to its lower content, relatively lesser diffraction intensity and lower crystallinity. The diffraction peaks of rGO-CdS heterostructure appeared to be narrower and stronger as compared to pure CdS NPs, indicating the enhanced crystallinity of pure CdS NPs [9,65,66].

The crystallite size of 22.18 nm and 54.23 nm was calculated for pure CdS NPs and rGO-CdS heterostructure, respectively using Scherrer's formula:

$$D = 0.9 \lambda / \beta \cos \theta$$

where, D is the crystallite size, λ is the wavelength of X-ray, β is the full width at half maxima (FWHM) and θ corresponds to the Bragg's angle.

The average crystallite size was enhanced from 22.18 nm to 54.23 nm showed that rGO sheets helped in the nucleation of CdS NPs on their surface and thereby, improved the crystallinity of pure CdS NPs [9,67].

The FTIR spectra of pure CdS NPs and rGO-CdS heterostructure are shown in Fig. 4(b). The FTIR pattern of pure CdS NPs exhibited distinctive absorption bands at 3466 cm^{-1} (OH stretching vibrations), 1623 cm^{-1} (C=C bonding), 1404 cm^{-1} (OH stretching vibrations of

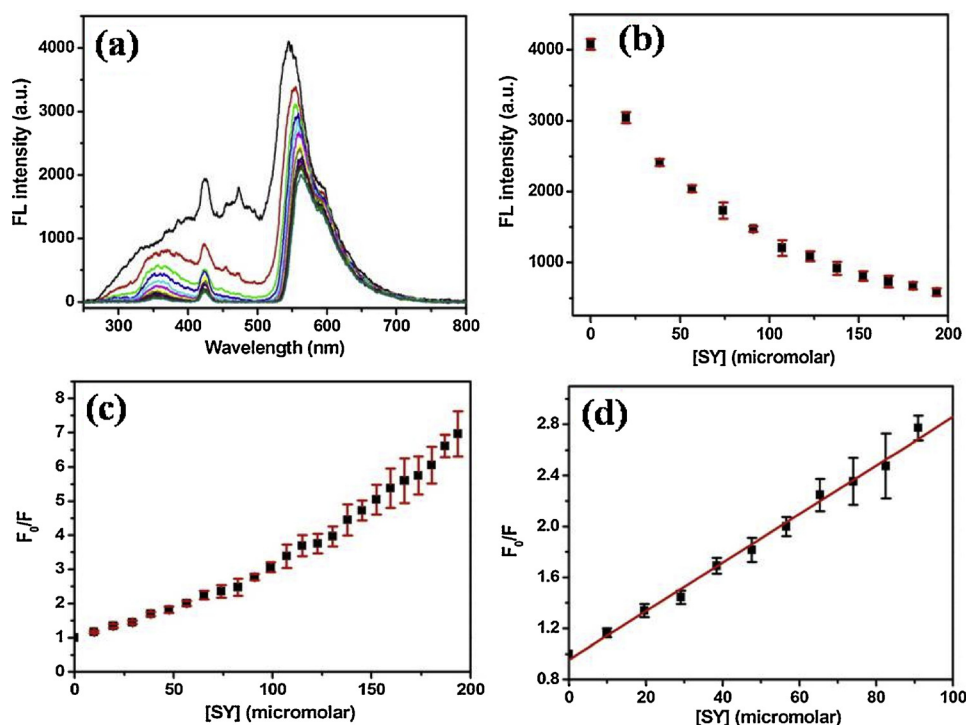


Fig. 13. (a) Decrease in FL emission intensity of rGO-CdS heterostructure (concentration: 0.20 mg/mL, volume: 1 mL) with increasing concentration of SY (from top to bottom: 0, 19.6, 38.46, 56.6, 74.07, 90.9, 107.14, 122.8, 137.93, 152.54, 166.66, 180.32, 193.54 μM) (b) Variation of FL intensity of rGO-CdS heterostructure with respect to change in SY concentration (c) Graph between F_0/F and different concentrations of SY (where F_0 and F refers to the FL emission intensity values at 545 nm in the absence and presence of SY) and (d) Stern Volmer quenching curve for the detection of SY using rGO-CdS heterostructure as a FL probe. The error bars are based on the triplicate experiments.

Table 1

Regression coefficient and detection limit for the FL sensing of Ag(I) and SY using rGO-CdS heterostructure.

Analyte	Regression coefficient	Detection limit (μM)
Ag(I)	0.99171	12.35
SY	0.99659	7.89

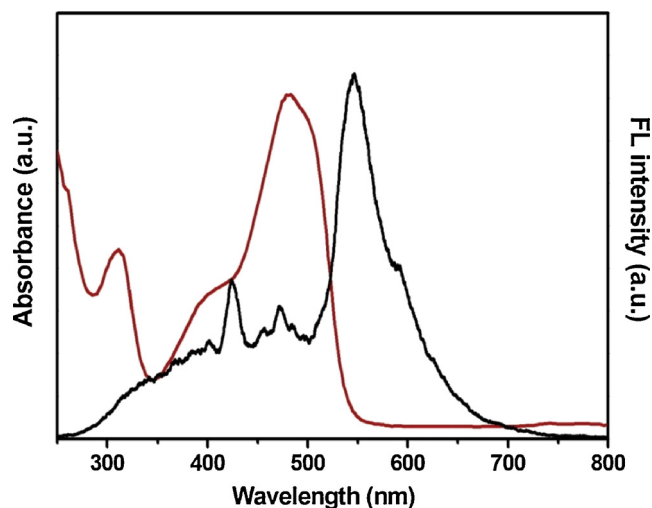


Fig. 14. Spectral overlap between FL emission curve of rGO-CdS heterostructure (black line) and UV-vis absorbance spectrum of SY (red line). (For interpretation of the references to colour in this figure legend, the reader is referred to the web version of this article).

carboxyl group), 1143 and 1013 cm^{-1} (C–O stretching vibrations/ plane bending vibrations of C–H bond), 651, 621 and 538 cm^{-1} (Cd–S stretching vibrations) [1,8,13,60,61,68]. The FTIR spectrum of rGO-CdS heterostructure exhibited much lower absorption intensity with respect to pure CdS NPs.

The surface and elemental composition of the prepared rGO-CdS

heterostructure was explored using XPS technique. The wide scan XPS spectrum of the prepared heterostructure revealed the existence of C, O, Cd and S elements without the presence of any impurities (Fig. 5).

The high resolution scan of C 1s exhibited binding energy peaks at 284.4 eV (C=C), 285.5 eV (C–O) and 286.7 eV (C–O–C) as depicted in Fig. 6(a) [69]. The XPS spectrum of Cd 3d displayed two doublet peaks at 405.2 eV and 412.0 eV assigned to the existence of Cd 3d_{5/2} and Cd 3d_{3/2}, respectively (Fig. 6(b)). The high resolution XPS spectrum of S 2p showed two major peaks at 161.5 eV and 162.7 eV ascribed to S 2p_{3/2} and S 2p_{1/2}, respectively (Fig. 6(c)). The XPS spectra of Cd 3d and S 2p confirmed the existence of Cd²⁺ and S^{2−} electronic states of CdS and the data was well matched with the reported literature [70,71]. A minor peak at 168.3 eV revealed the presence of oxidized sulphur species. The presence of oxidized sulphur species was consistent with the reported literature [72–74]. The high resolution O 1s could be resolved into three peaks at 530.7 eV, 531.7 eV and 533.1 eV (Fig. 6(d)). These three peaks were related to the presence of C–O, C=O and H–O–C=O functional groups, respectively [75,76].

Raman spectroscopy is an effective technique for the characterization of electronic and structural features of graphene based materials. The Raman spectrum of the prepared rGO-CdS heterostructure exhibited different characteristic peaks at 303, 574, 1316 and 1590 cm^{-1} as shown in Fig. 7(a). The peaks at 303 and 574 cm^{-1} were ascribed to the first order and second order longitudinal optical phonon mode of CdS NPs, respectively [61]. The peaks at 1316 and 1590 cm^{-1} were associated with D and G bands of rGO [61,77]. The D band is originated from the internal structural defects, edge defects on the hexagonal graphitic lattice and corresponded to the breathing mode of k-point phonons of A_{1g} symmetry. The G band arises from the in-plane stretching motion of sp² carbon bonds and assigned to the optical E_{2g} phonons at the Brillouin zone center.

FL spectroscopy is a useful technique to examine the surface defects and recombination rate of photogenerated electron and hole pairs. FL measurement of pure CdS NPs and rGO-CdS heterostructure was recorded at an excitation wavelength of 210 nm and FL emission peaks were obtained at 424 nm and 558 nm for pure CdS NPs. The FL spectra of pure CdS NPs and rGO-CdS heterostructure are shown in Fig. 7(b). A low intense FL emission peak at 424 nm was related to the

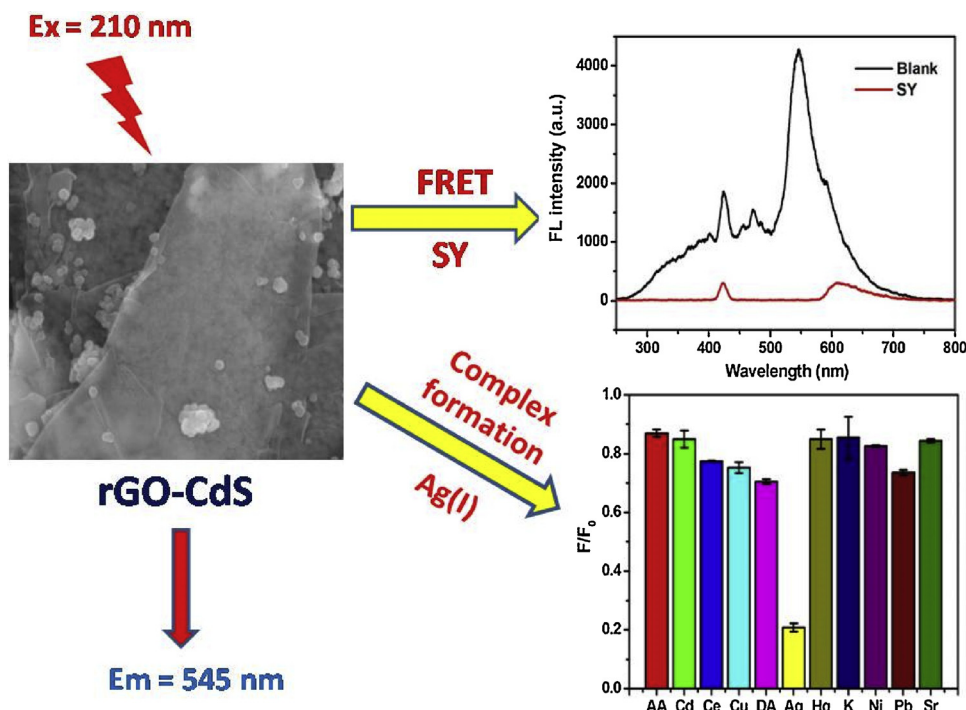


Fig. 15. Pictorial illustration for the sensing of Ag(I) and SY using rGO-CdS heterostructure as a FL probe.

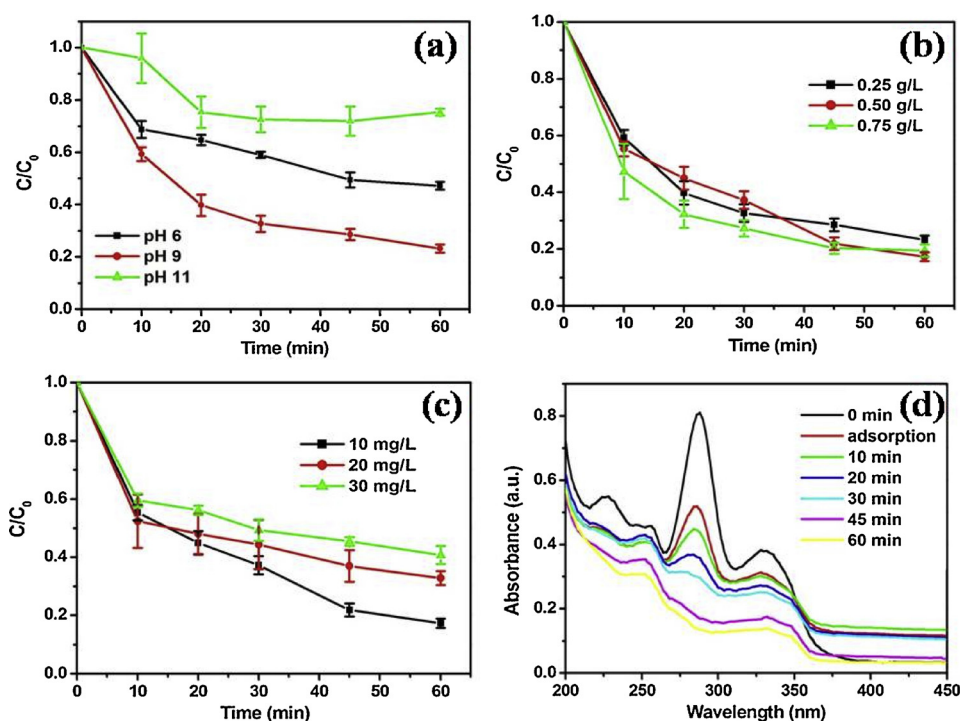


Fig. 16. Effect of (a) pH, (b) catalyst loading, (c) initial LVX concentration on the degradation efficiency of LVX in the presence of visible light using rGO-CdS heterostructure and (d) Time dependent absorbance spectra of LVX in the presence of rGO-CdS heterostructure at optimized operational parameters (pH: 9, catalyst dose: 0.50 g/L and initial LVX concentration: 10 mg/L). The error bars represent the standard deviations of triplicate (for a and b) and duplicate measurements (for c).

recombination of weakly trapped electron and hole pairs. However, a strong FL emission band at 558 nm was accredited to the band edge emission [78,79]. The intensity of FL emission peak was significantly diminished for rGO-CdS heterostructure. This behaviour can be accredited to the suppressed recombination rate of photogenerated charge carriers with facile transfer of electrons from CdS NPs to rGO sheets. The quenched FL intensity also showed the strong intimate interfacial contact between CdS NPs and rGO sheets and thereby, accountable for the excellent optoelectronic characteristics of the prepared heterostructure.

The UV-vis DRS measurements were recorded in the range of 200–800 nm in order to investigate the light harvesting efficiency of the prepared CdS NPs and rGO-CdS heterostructure. Fig. 8(a) shows the UV-vis DRS spectra of pure CdS NPs and rGO-CdS heterostructure. It was clearly seen that rGO-CdS heterostructure displayed a red shift in the absorption edge with respect to pure CdS NPs. The band gap of the prepared rGO-CdS heterostructure was computed from the empirical equation [80–83]:

$$(\alpha h\nu)^n = A(h\nu - E_g)$$

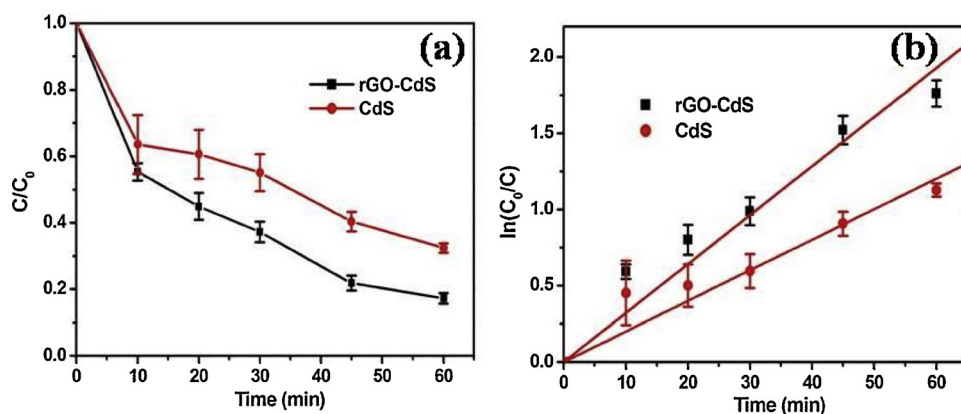


Fig. 17. (a) Comparison of degradation extent of LVX using pure CdS NPs and rGO-CdS heterostructure under visible light and (b) graph between $\ln(C_0/C)$ and time for the photocatalytic removal of LVX at optimized reaction parameters (pH: 9, catalyst dose: 0.50 g/L and initial LVX concentration : 10 mg/L). The error bars are based on standard deviations of triplicate measurements.

Table 2

Regression coefficient and rate constant values for the photocatalytic removal of LVX using pure CdS NPs and rGO-CdS heterostructure under visible light.

Photocatalyst	Regression coefficient	Rate constant (min^{-1})
rGO-CdS heterostructure	0.98245	0.03213
CdS NPs	0.97098	0.02005

where, α , $h\nu$, A and E_g corresponds to the absorption coefficient, photonic energy, proportionality constant and band gap energy, respectively. The value of n is dependent on optical transition of the material and for allowed direct transition, the value of n is considered as 2. The graph between $(\alpha h\nu)^2$ and $h\nu$ is illustrated in Fig. 8(b) and band gap energies were calculated to be around 2.26 eV and 2.16 eV for pure CdS NPs and rGO-CdS heterostructure, respectively. The UV-vis DRS results displayed enhanced light harvesting tendency of the prepared heterostructure towards the visible region as compared to pure CdS NPs. The reduction in the band gap of rGO-CdS heterostructure could be assigned to the charge delocalization from electronic interactions and chemical bonding between CdS NPs and rGO sheets.

The large specific surface area of the heterostructure provides more surface active sites, promotes the charge transportation and thereby, responsible for the enhanced photocatalytic performance. The nitrogen physisorption isotherm and the pore size distribution curves of the prepared rGO-CdS heterostructure are shown in Fig. 8(c and d). The total pore volume and specific surface area for rGO-CdS heterostructure were found to be $6.293 \times 10^{-2} \text{ cm}^3/\text{g}$ and $23.243 \text{ m}^2/\text{g}$, respectively. A pore radius of 1.43 nm was obtained using the density functional theory (DFT) method for the synthesized rGO-CdS heterostructure.

The thermal stability of pure CdS NPs and rGO-CdS heterostructure was investigated using TGA. The total weight loss of 42.7% and 25.82%

was observed in the entire temperature range for pure CdS NPs and rGO-CdS heterostructure, respectively. The TGA thermogram for pure CdS NPs is displayed in Fig. S2. The minor weight loss upto 800°C was due to the evaporation of physically adsorbed water molecules from the surface of CdS NPs. An abrupt weight loss (37%) was occurred above 800°C due to the decomposition of CdS NPs [1]. However, the TGA curve of rGO-CdS heterostructure showed enhanced thermal stability with respect to pure CdS NPs (Fig. 9). An approximate weight loss of 24% was found for the synthesized rGO-CdS heterostructure above 800°C . In the literature, it is reported that rGO possesses excellent thermal stability due to the removal of residual water molecules and only few oxygen containing functional groups are remained at the interlayered rGO surface [84,85]. It was observed from HRTEM and FESEM micrographs that pure CdS NPs were firmly bound to the surface of rGO sheets which improves the thermal stability of the synthesized heterostructure.

3.2. Sensing of Ag(I) and SY using rGO-CdS heterostructure as a FL probe

The prepared rGO-CdS heterostructure was employed for the FL sensing of transition metal ion; Ag(I) and synthetic food colorant; SY. The effect of metal ions and certain organic compounds on the FL intensity of rGO-CdS heterostructure was examined by measuring the FL intensity in the absence and presence of these interfering substances. The FL intensity of rGO-CdS heterostructure was substantially quenched with the addition of Ag(I) and SY as compared to other substances as shown in Fig. 10(a). Therefore, the prepared heterostructure displayed excellent selectivity towards the determination of Ag(I) and SY. Fig. 10(b) displays the impact of various competitive substances including AA, Cd, Ce, Cu, DA, Ag, Hg, K, Ni, Sr, Pb on the FL intensity ratio (F/F_0) of the rGO-CdS heterostructure. It was found that the prepared FL probe showed outstanding selectivity towards the

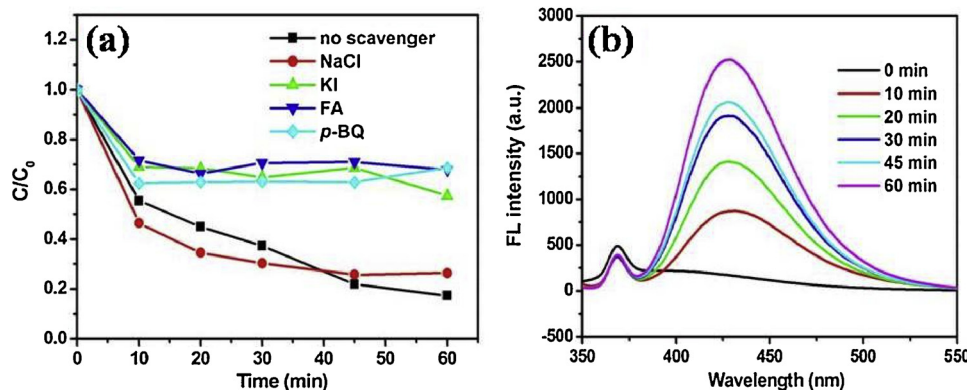


Fig. 18. (a) Photocatalytic decomposition of LVX over rGO-CdS heterostructure in the presence of different scavengers and (b) FL emission spectra of TA using rGO-CdS heterostructure under visible light illumination.

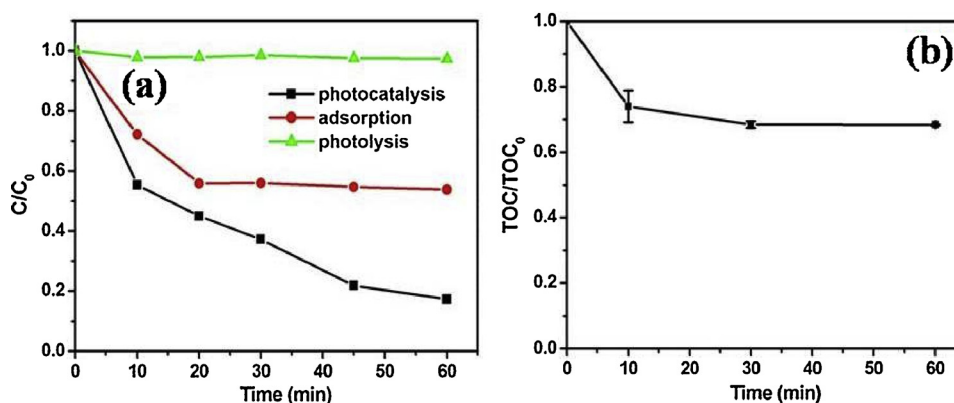


Fig. 19. (a) Comparison of different processes including photocatalysis, adsorption and photolysis for the removal of LVX and (b) Change in the TOC values for the decomposition of LVX using rGO-CdS heterostructure with respect to irradiation time.

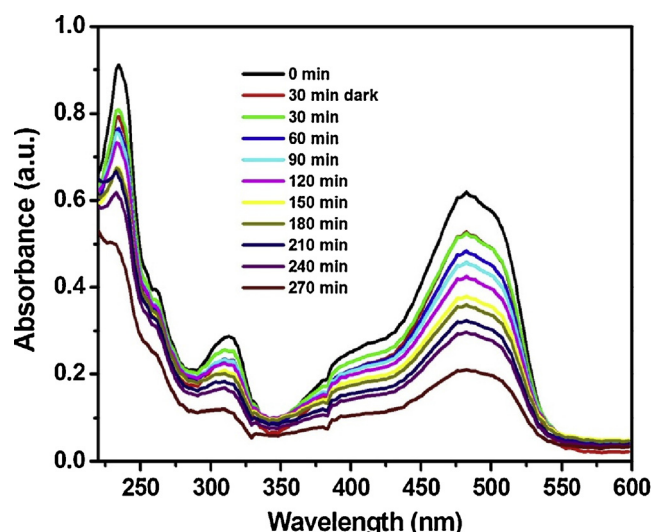


Fig. 20. Photocatalytic decomposition of SY over rGO-CdS heterostructure in the presence of visible light (catalyst dose: 0.50 g/L, initial SY concentration: 10 mg/L and natural pH).

detection of Ag(I).

The specificity of the prepared FL sensor for the monitoring of Ag(I) in the presence of different competitive substances was also explored as illustrated in Fig. 11(a). It was observed that the addition of different competitive substances showed no interference for the FL sensing of Ag(I) and thereby, confirmed the specific behaviour of the rGO-CdS heterostructure. Further, Fig. 11(b) indicates that the FL intensity of rGO-CdS heterostructure at $\lambda_{\max} \sim 545$ nm was decreased gradually with the increasing concentration of Ag(I). Fig. 11(c) depicts that the FL intensity was significantly diminished with increasing concentration of Ag(I) ranging from 0 to 193.54 μ M. The quenching behavior was analyzed using Stern-Volmer equation as shown below:

$$F_0/F = 1 + K_{SV}[C]$$

where, F_0 and F corresponds to the FL emission intensities of the probe at 545 nm in the absence and presence of the quencher (Ag(I) or SY), respectively, K_{SV} represents the Stern Volmer constant and C is the concentration of quencher.

Fig. 11(d) represents the calibration graph between F_0/F (where F_0 and F are the FL emission intensities at 545 nm in the absence and presence of Ag(I), respectively) and concentration of Ag(I). The detection limit was obtained from $3\sigma/m$, where σ and m represents the standard deviation and slope of the calibration plot, respectively. The linear working range and detection limit for the sensing of Ag(I) were

found to be 0–90.9 μ M and 12.35 μ M, respectively.

The as-formed rGO-CdS heterostructure was also utilized as an excellent sensor for the detection of food colorant, SY. The FL emission intensity curves of the rGO-CdS heterostructure in the presence of SY and TZ are shown in Fig. 12(a). The intensity of the FL emission peak was noticeably diminished in the presence of SY. It was found that the FL emission peak of the rGO-CdS heterostructure was substantially red shifted from 545 nm to 607 nm with the addition of SY. Fig. 12(b) depicts the change in FL intensity of the rGO-CdS heterostructure in the presence of SY and other representative species. It was clearly noticed that the representative species posed no interference towards the determination of SY. Thus, the prepared sensor displayed high specificity towards the successful detection of SY.

The capability of as-prepared rGO-CdS heterostructure towards the quantification of SY was examined by adding different concentrations of SY to the FL probe as shown in Fig. 13(a). With the increase in SY concentration, the FL intensity of rGO-CdS heterostructure at $\lambda_{\max} \sim 545$ nm was found to be remarkably quenched with the simultaneous red shift in the emission spectrum. Fig. 13(b) represents the effect of concentration of SY on the FL intensity of the prepared probe and it was observed that the FL intensity was strongly decreased. The relationship between F_0/F and SY concentration is demonstrated in Fig. 13(c). It was found that the FL intensity ratio of rGO-CdS heterostructure were linearly quenched at lower SY concentrations and deviated from linearity at higher concentrations. Fig. 13(d) exhibits the graph between F_0/F (where F_0 and F indicates the FL emission intensities in the absence and presence of SY at 545 nm) and SY concentration. A good linearity for SY was found to be in the concentration range of 0–90.9 μ M and detection limit was calculated to be as low as 7.89 μ M.

Table 1 demonstrates the values of regression coefficient and detection limit obtained for the quantification of Ag(I) and SY by employing GO-CdS heterostructure as a FL probe.

3.2.1. Proposed mechanism for the FL detection of Ag(I) and SY with rGO-CdS heterostructure

The strong FL intensity of rGO-CdS heterostructure was significantly reduced with the addition of Ag(I) and SY. It was reported in the literature that FL quenching was strongly dependent upon the charge density of the metal ion. Ag(I) possesses the smallest charge density as compared to other transition metal ions employed here and thereby, quenched the FL intensity to the maximum extent with respect to other transition metal ions. Moreover, Ag(I) and S^{2-} belong to soft acid and soft base, respectively. The soft acids have strong binding affinity towards soft bases according to hard soft acid base principle. Thus, the complex formation between Ag(I) and S^{2-} might be responsible for the FL quenching of the prepared rGO-CdS heterostructure [86]. The quenching of rGO-CdS heterostructure in the presence of SY can be explained through fluorescence resonance energy transfer (FRET)

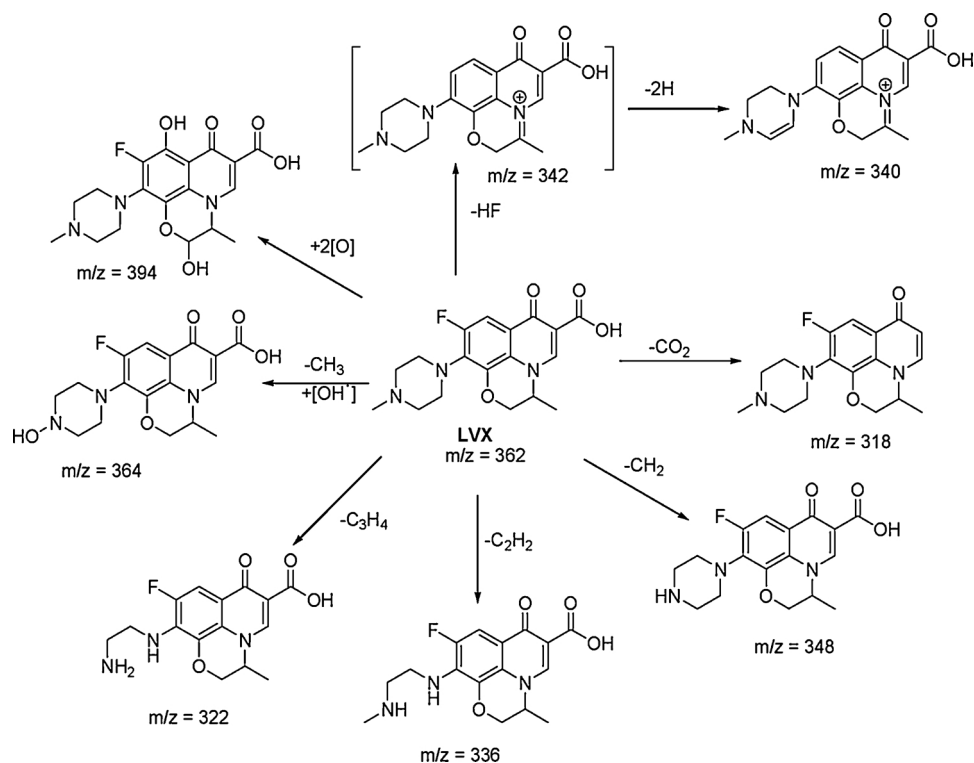


Fig. 21. Proposed reaction pathway for the degradation of LVX using rGO-CdS heterostructure in the presence of visible light.

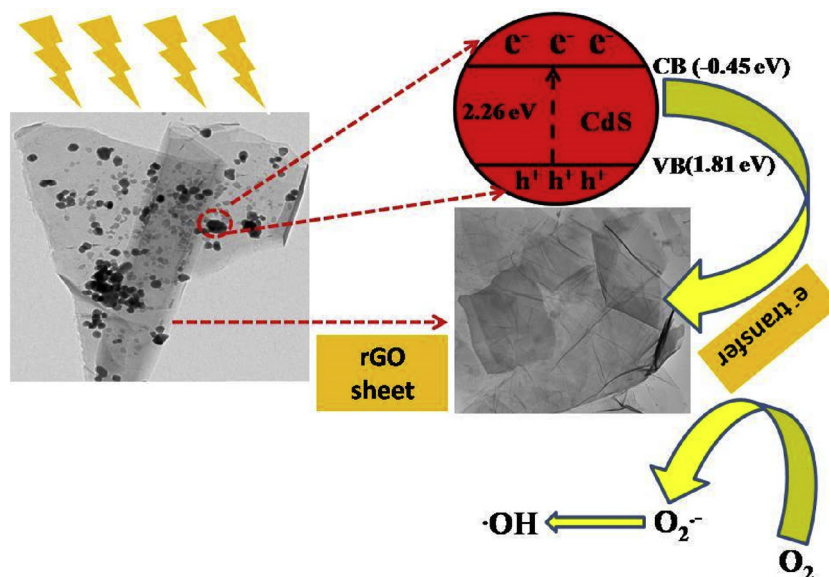


Fig. 22. Schematic representation of the mechanism for the photocatalytic degradation process using rGO-CdS heterostructure in the presence of visible light irradiation.

mechanism. The UV–vis absorbance spectrum of SY exhibited two maximum absorbance peaks at 311 and 482 nm and an intense FL emission peak of as-prepared rGO-CdS heterostructure was obtained at 545 nm (Fig. 14). A small spectral overlap was occurred between the FL emission spectrum of donor (rGO-CdS heterostructure) and UV–vis absorbance spectrum of acceptor (SY), suggesting the contribution of FRET mechanism towards the selective quenching of SY [87]. The pictorial representation for the FL sensing of Ag(I) and SY using rGO-CdS heterostructure is presented in Fig. 15.

3.3. Photocatalytic decomposition of FQ antibiotic; LVX over rGO-CdS heterostructure in the presence of visible light irradiation

The photocatalytic activity of the prepared rGO-CdS heterostructure was evaluated for the degradation of LVX under visible light illumination. The influence of pH on the photocatalytic decomposition of LVX was explored by changing the pH of the LVX solution from 6 to 11 at fixed amount of catalyst (0.25 g/L) and drug concentration (10 mg/L) as shown in Fig. 16(a). The removal efficiencies of 52.8%, 76.8% and 24.6% were acquired at pH 6, 9 and 11, respectively. The maximum degradation rate for LVX using rGO-CdS heterostructure was found to be at pH 9. The impact of solution pH on the photocatalytic

decomposition of FQs is a complex issue and is dependent on several factors such as ionization states of the photocatalyst, substrates and the rate of formation of radicals. LVX exists as a zwitterion in the pH range of 5.7–7.9. During the photocatalytic reactions, the positive holes are the major oxidation species in an acidic environment. However, in alkaline conditions, $\cdot\text{OH}$ plays a significant role towards the photocatalytic degradation of organic contaminants. In our case, the maximum degradation for LVX using rGO-CdS heterostructure was found to be at pH 9. An increase in the photocatalytic degradation efficiency with increasing pH from 6 to 9 can be assigned to the generation of highly reactive $\cdot\text{OH}$. After pH 9, the degradation rate was reduced with further increase in pH. It can be related to the more generation of $-\text{OH}$ ions which adsorbed on the surface of the photocatalytic material and thereby, making it negatively charged. Thus, an interaction between neutral or electron rich form of the drug and negatively charged surface photocatalyst was not favorable and thereby, degradation efficiency was reduced at pH 11 [88–91].

Fig. 16(b) describes the effect of catalyst amount towards the degradation of LVX at pH 9 and LVX concentration of 10 mg/L. It was found that the decomposition rate was significantly increased from 76.8% to 82.7% with the increment in catalyst dose from 0.25 g/L to 0.50 g/L. The degradation efficiency was then diminished to 80.6% with the further increase in catalyst dose up to 0.75 g/L. This is due to the presence of less number of active sites on the surface of the heterostructure for the photocatalytic reaction. The impact of initial LVX concentration on the degradation efficiency was also studied at pH 9 and catalyst dose of 0.50 g/L. The degradation rates were decreased with the increase in substrate concentration in the following sequence: 82.7% > 67.1% > 59.2% (Fig. 16(c)). The UV–vis absorbance spectrum for the photocatalytic decomposition of LVX with respect to time is represented in Fig. 16(d). The characteristic absorbance peak of LVX at $\lambda_{\text{max}} = 286 \text{ nm}$ was gradually decreased with the increase in irradiation time using rGO-CdS heterostructure. Around 82.7% degradation of LVX was acquired in illumination time of 60 min.

Furthermore, the photocatalytic activity of the prepared rGO-CdS heterostructure towards the degradation of LVX was compared with pure CdS NPs under optimized operational parameters (0.50 g/L photocatalyst amount, 10 mg/L LVX initial concentration and solution pH 9.0). The degradation rates of 67.5% and 82.7% were obtained for pure CdS NPs and rGO-CdS heterostructure, respectively as shown in Fig. 17(a). The XRD diffractogram of pure CdS NPs and rGO-CdS heterostructure depicted the existence of mixed crystal phases which exhibited higher photocatalytic activity and anti-photocorrosion features with respect to the single phase [92]. The synthesized rGO-CdS heterostructure executed enhanced photocatalytic degradation with respect to pure CdS NPs. The reinforced photocatalytic performance of the rGO-CdS heterostructure with respect to pure CdS NPs could be accounted to the enhanced visible light harvesting tendency, efficient charge separation and transportation of photoexcited charge carriers across the heterojunctional interface. The photocatalytic reaction kinetics for the degradation of LVX using pure CdS NPs and rGO-CdS heterostructure was also investigated (Fig. 17(b)). It was found that the photocatalytic decomposition of LVX in the presence of pure CdS NPs and rGO-CdS heterostructure fitted well with the pseudo first order kinetics model.

The regression coefficient and rate constant for the photocatalytic oxidation of LVX over pure CdS NPs and rGO-CdS heterostructure under visible light irradiation is shown in Table 2. The rate constant for rGO-CdS heterostructure was found to be higher with respect to pure CdS NPs.

The impact of various scavengers towards the photocatalytic degradation of LVX was also investigated (Fig. 18(a)). The removal efficiencies of 82.7%, 73.6%, 32.1%, 31.3% and 42.5% were obtained using no scavenger, NaCl, FA, BQ, and KI, respectively. A small reduction in the degradation extent was found with the addition of NaCl and indicated that h^+ played only a minor role towards the degradation

of LVX. The degradation efficiency was significantly quenched in the presence of FA, BQ, and KI and verified that the photocatalytic degradation of LVX is mainly driven by e^- , O_2^- and $\cdot\text{OH}_s$ species. The role of $\cdot\text{OH}$ in the degradation process was confirmed by employing TA as a probe molecule as depicted in Fig. 18(b). The reaction of $\cdot\text{OH}$ with TA formed fluorescent active species; 2-hydroxyterephthalic acid which exhibited FL emission peak at 427 nm. The intensity of FL emission peak at 427 nm was remarkably enhanced with the increase in visible light irradiation time and therefore, depicted the generation of $\cdot\text{OH}$ [1]. Therefore, it was concluded that e^- , O_2^- , $\cdot\text{OH}_s$ and $\cdot\text{OH}$ reactive species played an imperative role towards the degradation of LVX using rGO-CdS heterostructure.

Fig. 19(a) exhibits the comparison of photolysis, adsorption and photocatalysis processes for the removal of LVX. Adsorption experiment was conducted using rGO-CdS heterostructure in the absence of light source and it was found that 45.7% of LVX was adsorbed on the surface of the heterostructure. The photolysis experiment indicated the slight degradation (2.71%) of LVX in the presence of visible light irradiation. The degradation rate of 82.7% was achieved in the presence of rGO-CdS heterostructure under visible light. The mineralization of LVX was measured by performing TOC analysis (Fig. 19(b)). An initial TOC value of 10 mg/L LVX solution was found to be 6.752 mg/L and after the photocatalytic reaction of 60 min, the TOC value was reduced to 4.619 mg/L. Approximate 31.5% mineralization rate of LVX was achieved with rGO-CdS heterostructure under visible light in 60 min. Chen et al. [93] synthesized TiO_2 nanobelts decorated by bimetallic Au-Pd nanoparticles (Au-Pd/ TiO_2 NBs) and utilized for the photocatalytic degradation of LVX (5 mg/L, 35 mL). The degradation efficiency of 95% was obtained after 60 min of simulated solar light irradiation and 55% of TOC removal was attained in the same time period. Wang et al. [94] reported the complete removal of LVX in 60 min using Fe_3O_4 -graphite composite/ H_2O_2 system with the TOC removal rate of 48%. In this case, H_2O_2 was added to the reaction mixture for the generation of $\cdot\text{OH}$ and therefore, photocatalytic degradation efficiency was enhanced. Sharma et al. [95] completely degraded LVX (10 mg/L, 100 mL) in 90 min of sunlight illumination using $\text{TiO}_2/\text{C-dots}$ composite with the TOC removal rate of 53.4%. In another study, anodic oxidation (AO), AO with electrogenerated H_2O_2 (AO- H_2O_2) and electro-Fenton (EF) processes were employed by Gong et al. [96] for the mineralization of LVX (200 mg/L, 500 mL) using an activated carbon fiber (ACF) felt cathode. Under the similar experimental conditions, the degradation efficiencies of 72% and 90% were obtained in the reaction time of 120 min using AO and AO- H_2O_2 , respectively. The complete removal of LVX was acquired with EF process due to the more generation of $\cdot\text{OH}$. The TOC removal rates of 13%, 27% and 61% were achieved with AO, AO- H_2O_2 , and EF processes; respectively in the reaction time of 360 min. Therefore, it can be concluded that our results are comparable with the already existing literature.

The photocatalytic activity of the fabricated rGO-CdS heterostructure was also explored for the degradation of SY under visible light. The degradation rate of 66% was achieved for SY using rGO-CdS heterostructure after exposure to visible light for 270 min. The characteristic absorbance peak of SY at 482.4 nm was remarkably quenched with the increase in illumination time as displayed in (Fig. 20). Therefore, the prepared heterostructure executed high efficiency for the photocatalytic decomposition of FQ and synthetic food colorant.

3.4. Identification of transformation products based on photocatalytic degradation of LVX

The transformation products of LVX were identified using LCMS analysis and the structural identification of the products was based on the inspection of molecular ion peaks $[\text{M} + \text{H}]^+$. The formed reaction intermediates are shown in Fig. S3(a–d). The protonated ion peak of the parent compound LVX was appeared at m/z 362 with the molecular formula ($\text{C}_{18}\text{H}_{20}\text{FN}_3\text{O}_4$) and molecular weight ($M = 361.368 \text{ g/mol}$). A

fragmented peak at m/z 348 corresponded to the demethylation of the piperazinyl ring with the formation of secondary amine [97]. The peaks at m/z 322 and m/z 318 were ascribed to the loss of C_3H_4 and CO_2 from the parent compound [94,96]. A peak at m/z 336 was assigned to the partial elimination of piperazinyl ring from the LVX structure [94]. A peak at m/z 364 was related to the generation of hydroxylamine at the N-piperazine position due to the ring opening (de-methylation) followed by hydroxylation [52]. A peak at m/z 394 indicated the formation of dihydroxylated product [52]. A peak centered at m/z 342 was attributed to the defluorination of LVX which was further oxidized to m/z 340 [94,98]. The transformation products of LVX and the plausible degradation pathway using rGO-CdS heterostructure are shown in Fig. 21.

3.5. Plausible mechanism for the degradation of LVX using rGO-CdS heterostructure

The conduction band (CB) and valence band (VB) potentials of pure CdS NPs can be computed using the following equations:

$$E_{VB} = X - E_e + 0.5 E_g$$

$$E_{CB} = E_{VB} - E_g$$

where X is the absolute electronegativity of CdS NPs; E_e is the energy of free electrons on the hydrogen scale (~ 4.5 eV) and E_g is the band gap of CdS NPs. The value of X for CdS NPs was reported to be 5.18 eV. The band gap, CB and VB potentials of CdS NPs were measured to be 2.26 eV, -0.45 eV and 1.81 eV, respectively. Fig. 22 demonstrates the pictorial representation of the photocatalytic degradation process under visible light. When the surface of rGO-CdS heterostructure was subjected to light irradiation, the photoexcited e^- and h^+ were generated in the CB and VB of pure CdS NPs, respectively. The photogenerated e^- in the CB of CdS NPs were then transferred to the surface of rGO and reacted with adsorbed molecular oxygen to yield $O_2^{\cdot -}$ which further participated in various redox reactions to generate $\cdot OH$. However, the photogenerated h^+ in the VB of CdS NPs cannot react with water to yield $\cdot OH$ because the value of VB potential of CdS NPs (1.81 eV) is lower than the standard $E^\circ(OH^\cdot/OH) = 1.99$ eV. Therefore, e^- , $O_2^{\cdot -}$ and $\cdot OH$ played a significant role towards the degradation of LVX using rGO-CdS heterostructure in the presence of visible light as also confirmed from scavenger study.

4. Conclusions

In summary, rGO-CdS heterostructure was prepared through a hydrothermal method and morphological, structural, optical, textural and thermal characteristics of the synthesized heterostructure have been investigated in detail. The synthesized rGO-CdS heterostructure was employed as an effective FL sensor for the specific determination of Ag (I) and SY. The photocatalytic capability of the rGO-CdS heterostructure was explored for the degradation of LVX and SY in the presence of visible light. The degradation rate of 82.7% was acquired for LVX after exposure to visible light irradiation for 60 min. Therefore, the rGO-CdS heterostructure can be potentially explored as a wonderful sensing and visible light responsive photocatalytic material in terms of environmental remediation.

Acknowledgements

This work was financially supported by AICTE MODROB (File No. 9-181/RIFD/MODROB/policy-1/2016-17) and TEQIP-III project grant of Dr. S.S. Bhatnagar University Institute of Chemical Engineering and Technology, Panjab University, Chandigarh. Manjot Kaur would like to thank UGC, Government of India for awarding fellowship under UGC-BSR scheme (Grant No. F. 25-1/2014-15(BSR)/No. F. 5-91/2007/(BSR)). The authors would like to appreciate Sophisticated Analytical

Instrumentation Facility (SAIF), Panjab University, Chandigarh, National Institute of Pharmaceutical Education and Research, S.A.S. Nagar, Mohali and Materials Research Centre, MNIT, Jaipur for the extensive characterization of the prepared samples.

Appendix A. Supplementary data

Supplementary material related to this article can be found, in the online version, at doi:<https://doi.org/10.1016/j.apcatb.2018.12.042>.

References

- [1] M. Kaur, S.K. Mehta, S.K. Kansal, J. Environ. Chem. Eng. 6 (2018) 3631–3639.
- [2] M.Z. Selcuk, F. Ongul, M.S. Boroglu, I. Boz, S.A. Yuksel, J. Nanoelectron. Optoelectron. 12 (2017) 642–650.
- [3] S. Kaveri, L. Thirugnanam, M. Dutta, J. Ramasamy, N. Fukata, Ceram. Int. 39 (2013) 9207–9214.
- [4] T. Zhang, W. Yang, Q. Yang, P. Yang, W. Sun, Sci. Adv. Mater. 10 (2018) 1489–1497.
- [5] D.C. Onwudiwe, T. Arfin, C.A. Strydom, Electrochim. Acta 116 (2014) 217–223.
- [6] C.I.I. Park, N.-H. Kim, Sci. Adv. Mater. 10 (2018) 232–237.
- [7] S. Wageh, A.A. Al-Ghamdi, Y. Al-Turki, N. Al-Senany, F. Yakuphanoglu, J. Nanoelectron. Optoelectron. 12 (2017) 260–266.
- [8] Y. Tang, X. Liu, C. Ma, M. Zhou, P. Huo, L. Yu, J. Pan, W. Shi, Y. Yan, New J. Chem. 39 (2015) 5150–5160.
- [9] Q. Li, B. Guo, J. Yu, J. Ran, B. Zhang, H. Yan, J.R. Gong, J. Am. Chem. Soc. 133 (2011) 10878–10884.
- [10] Y.A.-K. Kalandaragh, F.S.-B. Bodagh, E.A.-G. Gheshlaghi, A. Khodayari, J. Nanoelectron. Optoelectron. 12 (2017) 231–235.
- [11] P. Gao, J. Liu, S. Lee, T. Zhang, D.D. Sun, J. Mater. Chem. 22 (2012) 2292–2298.
- [12] H.K. Dhandu, M. Kaur, G. Singh, J. Nanoelectron. Optoelectron. 12 (2017) 247–253.
- [13] N. Qutub, B.M. Pirzada, K. Umar, S. Sabir, J. Environ. Chem. Eng. 4 (2016) 808–817.
- [14] Y. Fan, Z. Wu, T. Sun, H. Zhan, W. Liu, S. Bi, Sci. Adv. Mater. 10 (2018) 1729–1736.
- [15] D. Kim, D. Jung, J. Kyun Noh, J.-H. Han, Sci. Adv. Mater. 10 (2018) 1268–1273.
- [16] F. Lv, H. Wang, Z. Li, Q. Zhang, X. Liu, Y. Su, Front. Environ. Sci. Eng. 12 (2018) 4.
- [17] Y. Li, Z. Sun, S. Zhu, Y. Liao, Z. Chen, D. Zhang, Carbon 94 (2015) 599–606.
- [18] M. Rakiuddin, S. Mandal, R. Ananthakrishnan, New J. Chem. 41 (2017) 1380–1389.
- [19] G. Nam, J.-Y. Leem, Sci. Adv. Mater. 10 (2018) 405–409.
- [20] X. Cui, L. Zhu, J. Wu, Y. Hou, P. Wang, Z. Wang, M. Yang, Biosens. Bioelectron. 63 (2015) 506–512.
- [21] M. Kaur, S.K. Mehta, S.K. Kansal, Sens. Actuators B 245 (2017) 938–945.
- [22] M. Kaur, S.K. Mehta, S.K. Kansal, Spectrochim. Acta Part A 180 (2018) 37–43.
- [23] F. Jafari, A. Salimi, A. Navaee, Electroanalysis 26 (2014) 1782–1793.
- [24] P.S. Dorraji, F. Jalali, Food Chem. 227 (2017) 73–77.
- [25] Y. Su, S. Yang, W. Liu, L. Qiao, J. Yan, Y. Liu, S. Zhang, Y. Fang, Microchim. Acta 184 (2017) 4065–4072.
- [26] O.K. Okoth, K. Yan, J. Zhang, Carbon 120 (2017) 194–202.
- [27] K.A. Zeynali, S.M. Khoshmanesh, J. Chin. Chem. Soc. 62 (2015) 772–779.
- [28] D.L. Giokas, G.Z. Tsogas, A.G. Vlessidis, M.I. Karayannis, Anal. Chem. 76 (2004) 1302–1309.
- [29] S. Hu, S. Zhang, Z. Hu, Z. Xing, X. Zhang, Anal. Chem. 79 (2007) 923–929.
- [30] S.A. Oehle, J. Chromatogr. A 745 (1996) 233–237.
- [31] K. Sato, S. Tanaka, Microchem. J. 53 (1996) 93–98.
- [32] S. Li, Y. Li, J. Cao, J. Zhu, L. Fan, X. Li, Anal. Chem. 86 (2014) 10201–10207.
- [33] X. Sun, P. Liu, L. Wu, B. Liu, Analyst 140 (2015) 6742–6747.
- [34] H. Chakraborti, S. Sinha, S. Ghosh, S.K. Pal, Mater. Lett. 97 (2013) 78–80.
- [35] Z.S. Qian, X.Y. Shan, L.J. Chai, J.R. Chen, H. Feng, Biosens. Bioelectron. 68 (2015) 225–231.
- [36] P. Su, Z. Zhu, J. Wang, B. Cheng, W. Wu, K. Iqbal, Y. Tang, Sens. Actuators B 273 (2018) 93–100.
- [37] H. Wu, J. Jia, Y. Xu, X. Qian, W. Zhu, Sens. Actuators B 265 (2018) 59–66.
- [38] B.Y. Zhu, M. Xu, C.-X. Qian, L. Han, J.-R. Gao, Q. Ye, Y.-J. Li, Res. Chem. Intermed. 44 (2018) 3985–3999.
- [39] M.R. Majidi, M.H.P. Azar, R.F.B. Baj, A. Naseri, Ionics 21 (2015) 863–875.
- [40] M. Arvand, Z. Erfanifar, M.S. Ardaki, Food Anal. Methods 10 (2017) 2593–2606.
- [41] L. Yu, M. Shi, X. Yue, L. Qu, Sens. Actuators B 209 (2015) 1–8.
- [42] B. Thirumalraj, C. Rajkumar, S.-M. Chen, P. Veerakumar, P. Perumal, S.-B. Liu, Sens. Actuators, B 257 (2018) 48–59.
- [43] H. Yang, Y. Long, H. Li, S. Pan, H. Liu, J. Yang, X. Hua, J. Colloid Interface Sci. 516 (2018) 192–201.
- [44] Y.Z. Song, Can. J. Chem. 88 (2010) 676–681.
- [45] L. Yu, M. Shi, X. Yue, L. Qu, Sens. Actuators B 225 (2016) 398–404.
- [46] M.R. Majidi, R.F.B. Baj, A. Naseri, Food Anal. Methods 6 (2013) 1388–1397.
- [47] R.A. Medeiros, B.C. Lourencao, R.C. Rocha-Filho, O. Fatibello-Filho, Talanta 99 (2012) 883–889.
- [48] E. Dinc, E. Baydan, M. Kanbur, F. Onur, Talanta 58 (2002) 579–594.
- [49] R.S. Razmara, A. Daneshfar, R. Sahrai, J. Ind. Eng. Chem. 17 (2011) 533–536.
- [50] M. Sturini, A. Speltini, F. Maraschi, L. Pretali, E.N. Ferri, A. Profumo, Chemosphere 134 (2015) 313–318.

- [51] E.A.S. Galvis, S.D.J. Sierra, K.E.B. Perlaza, F. Ferraro, R.A.T. Palma, *Chem. Eng. J.* 315 (2017) 552–561.
- [52] Y. Li, D. Wei, Y. Dua, *Chemosphere* 119 (2015) 282–288.
- [53] X.V. Doorslaer, J. Dewulf, H.V. Langenhove, K. Demeestere, *Sci. Total Environ.* 500–501 (2014) 250–269.
- [54] J.-Q. Xiong, M.B. Kurade, B.-H. Jeon, *Chem. Eng. J.* 313 (2017) 1251–1257.
- [55] P. Tiaspaul, T. Miller, Strathmann, *Environ. Sci. Technol.* 41 (2007) 4720–4727.
- [56] P. Calza, C. Hadjicostas, V.A. Sakkas, M. Sarro, C. Minero, C. Medana, T.A. Albanis, *Appl. Catal. B* 183 (2016) 96–106.
- [57] L. Lin, H. Wang, P. Xu, *Chem. Eng. J.* 310 (2017) 389–398.
- [58] F. Liu, X. Shao, J. Wang, S. Yang, H. Li, X. Meng, X. Liu, M. Wang, *J. Alloys Compd.* 551 (2013) 327–332.
- [59] H. Liu, T. Lv, X. Wu, C. Zhu, Z. Zhu, *Appl. Surf. Sci.* 305 (2014) 242–246.
- [60] F.X. Xiao, J. Miao, B. Liu, *J. Am. Chem. Soc.* 136 (2014) 1559–1569.
- [61] N. Meng, Y. Zhou, W. Nie, P. Chen, *J. Nanopart. Res.* 18 (2016) 241.
- [62] L. Stobinski, B. Lesiak, A. Malolepszy, M. Mazurkiewicz, B. Mierzwa, J. Zemek, P. Jiricek, I. Bieloshapka, *J. Electron. Spectrosc. Relat. Phenom.* 195 (2014) 145–154.
- [63] M. Huang, J. Yu, Q. Hu, W. Su, M. Fan, B. Li, L. Dong, *Appl. Surf. Sci.* 389 (2016) 1084–1093.
- [64] L. Zhang, Y. Shi, L. Wang, C. Hu, *Appl. Catal., B* 220 (2018) 118–125.
- [65] L. Wang, M. Wen, W. Wang, N. Momuinou, Z. Wang, S. Li, *J. Alloys Compd.* 683 (2016) 318–328.
- [66] R. Bera, S. Kundu, A. Patra, *ACS Appl. Mater. Interfaces* 7 (2015) 13251–13259.
- [67] N. Jiang, Z. Xiu, Z. Xie, H. Li, G. Zhao, W. Wang, Y. Wu, X. Hao, *New. J. Chem.* 38 (2014) 4312–4320.
- [68] M.S. Arania, M.S. Niasari, *New. J. Chem.* 38 (2014) 1179–1185.
- [69] A. Malas, A. Bharati, O. Verkinderen, B. Goderis, P. Moldenaers, R. Cardinaels, *Polymers* 9 (2017) 613.
- [70] X. Yue, S. Yi, R. Wang, Z. Zhang, S. Qiu, *Sci. Rep.* 6 (2016) 22268.
- [71] J. Xu, L. Wang, X. Cao, *Chem. Eng. J.* 283 (2016) 816–825.
- [72] B. Quan, S.-Ho Yu, D.Y. Chung, A. Jin, J.H. Park, Y.-E. Sung, Y. Piao, *Sci. Rep.* 4 (2014) 5639.
- [73] W. Han, L. Chen, W. Song, S. Wang, X. Fan, Y. Li, F. Zhang, G. Zhang, W. Peng, *Appl. Catal., B* 236 (2018) 212–221.
- [74] M. Wu, Q. Tang, F. Dong, Z. Bai, L. Zhang, J. Qiao, *J. Catal.* 352 (2017) 208–217.
- [75] L. Zhang, Y. Li, L. Zhang, D.-W. Li, D. Karpuzov, Y.-T. Long, *Int. J. Electrochem. Sci.* 6 (2011) 819–829.
- [76] B. Yu, X. Wang, X. Qian, W. Xing, H. Yang, L. Ma, Y. Lin, S. Jiang, Lei Song, Y. Hu, S. Lo, *RSC Adv.* 4 (2014) 31782–31794.
- [77] W. Mu, Q. Yu, R. Hu, X. Li, H. Wei, Y. Jian, *Appl. Surf. Sci.* 423 (2017) 1203–1211.
- [78] S. Kumar, A.K. Ojha, *Mater. Chem. Phys.* 171 (2016) 126–136.
- [79] W. Liu, B. He, Z. He, G. He, *Asian J. Chem.* 24 (2012) 1465–1468.
- [80] Z. Han, Chen G, C. Li, Y. Yu, Y. Zhou, *J. Mater. Chem. A* 3 (2015) 1696–1702.
- [81] W. Xing, W. Tu, Z. Han, Y. Hu, Q. Meng, G. Chen, *ACS Energy Lett.* 3 (2018) 514–519.
- [82] Z. Han, G. Chen, C. Li, Y. Zhou, Y. Hu, W. Xing, *Inorg. Chem.* 57 (2018) 13067–13070.
- [83] W. Xing, C. Li, G. Chen, Z. Han, Y. Zhou, Y. Hu, Q. Meng, *Appl. Catal. B* 203 (2017) 65–71.
- [84] Y.J. Oha, J.J. Yoo, Y. Il Kim, J.K. Yoon, H.N. Yoon, J.-H. Kim, S.B. Park, *Electrochim. Acta* 116 (2014) 118–128.
- [85] I.K. Moon, J. Lee, R.S. Ruoff, H. Lee, *Nat. Commun.* 1:73 (2010), <https://doi.org/10.1038/ncomms1067>.
- [86] R. Tabaraki, A. Nateghi, *J. Fluoresc.* 26 (2016) 297–305.
- [87] Y. Yuan, X. Zhao, M. Qiao, J. Zhu, S. Liu, J. Yang, X. Hua, *Spectrochim. Acta Part A* 167 (2016) 106–110.
- [88] E. Hapeshi, I. Fotiou, D.F. -Kassinou, *Chem. Eng. J.* 224 (2013) 96–105.
- [89] W. Li, C. Guo, B. Su, Jian Xu, *J. Chem. Technol. Biotechnol.* 87 (2012) 643–650.
- [90] R. Molinari, F. Pirillo, V. Loddo, L. Palmisano, *Catal. Today* 118 (2006) 205–213.
- [91] N. Kunwar, R. Ameta, S. Sharma, *Sci. Revs. Chem. Commun.* 4 (2014) 124–129.
- [92] W.-C. Peng, Y. Chen, X.-Y. Li, *J. Hazard. Mater.* 309 (2016) 173–179.
- [93] Q. Chen, Y. Xin, X. Zhu, *Electrochim. Acta* 186 (2015) 34–42.
- [94] L. Wang, Q. Zhao, J. Hou, J. Yan, F. Zhang, J. Zhao, H. Ding, Y. Li, L. Ding, *J. Environ. Sci. Health Part A* 51 (2016) 52–62.
- [95] S. Sharma, A. Umar, S.K. Mehta, A.O. Ibhaddon, S.K. Kansal, *New J. Chem.* 42 (2018) 7445–7456.
- [96] Y. Gong, J. Li, Y. Zhang, M. Zhang, X. Tian, A. Wang, *J. Hazard. Mater.* 304 (2016) 320–328.
- [97] H. Wei, D. Hu, J. Su, K. Li, *Chin. J. Chem. Eng.* 23 (2015) 296–302.
- [98] P. Calza, C. Medana, F. Carbone, V. Giancotti, C. Baiocchi, *Rapid Commun. Mass. Spectrom.* 22 (2008) 1533–1552.